

Bifunctional Mn-Fe Oxide Catalysts for Zn-Air Battery Air Electrodes Fabricated Through Atomic Layer Deposition

Matthew Labbe,^[a] Michael P. Clark,^[a] Ken Cadien,^[a] and Douglas G. Ivey^{*[a]}

Zinc-air batteries (ZABs) are one of many energy storage technologies that can help integrate renewable energy into the power grid. A key developmental goal for ZABs is replacing the precious metal catalysts at the air electrode with more abundant and inexpensive materials. In this work, a MnFe_xO_y bifunctional catalyst is directly deposited on a ZAB air electrode using atomic layer deposition (ALD). With ALD, the atomic composition of the air electrode coating can be finely tuned based on catalytic activity. Characterization through electron microscopy, photoelectron spectroscopy and diffraction techniques indicate that the novel ALD film deposits as a nanocrystal-

line $(\text{Mn},\text{Fe})_3\text{O}_4$ cubic spinel. The mixed oxide catalyst outperforms its individual binary MnO_x or FeO_x constituents, operating at 52.5% bifunctional efficiency at 20 mA cm^{-2} . Moreover, the long term stability of the ALD catalyst is showcased by 600 h (1565 cycles) of ZAB cycling at 10 mA cm^{-2} . The efficiency retention of the bifunctional transition metal oxide catalyst is superior to a precious metal benchmark of Pt–Ru–C, with 84.7% efficiency retention after more than 1500 cycles versus only 66.2% retention for the precious metal catalyst. The ALD technique enables deep penetration of catalyst material into the air electrode structure, improving the cycling behaviour.

Introduction

Primary Zn-air batteries (ZABs), while not a new technology, have only ever penetrated the market for hearing-aids due to low power outputs from inefficient reaction kinetics.^[1,2] The main culprit is often identified as the oxygen reduction reaction (ORR) during battery discharge.^[3] For secondary ZABs, the oxygen evolution reaction (OER) during recharge is also sluggish and reduces overall battery efficiency.^[3] The use of an appropriate catalyst, however, can modify the reaction kinetics and improve the power yield of ZABs.^[4,5] The traditional catalyst for ORR is Pt, while that for OER is RuO_2 .^[1] These precious metal catalysts impede the practicality of ZABs and increase their potential cost. On the other hand, earth-abundant materials such as transition metal oxides can also be applied as ORR and OER catalysts and have sparked a tremendous growth in research.^[1,5,6] Furthermore, a bifunctional catalyst, active towards both ORR and OER, is highly desirable and can often be achieved using a combination of several transition metal oxides.^[4,5] These bifunctional transition metal oxide catalysts are also more stable than their precious metal counterparts during prolonged battery cycling.^[7–9] Mn oxides (MnO_x) are the most common candidates for ORR catalysis, while OER catalysts

include the oxides of Co, Ni, and Fe.^[5,10,11] Among these options, Mn and Fe are found in the greatest abundance in the earth^[12] and at the lowest industrial cost.^[13] Thus, mixed oxides of Mn and Fe have been well explored in the literature as OER,^[14,15] ORR,^[16] and bifunctional catalysts.^[17,18] However, the application of these particular oxides in ZABs is rare.^[8,19,20]

In ZABs, ORR and OER occur at the air electrode, a porous membrane that allows oxygen exchange between the battery cell and the ambient environment (Figure 1). This membrane, usually carbon based, is often called the gas diffusion layer (GDL) and is composed of two distinct layers. The air facing side, called the backing layer, features large porosity for oxygen flow and a hydrophobic treatment, often with polytetrafluoroethylene (PTFE), to prevent electrolyte loss. The electrolyte facing side, called the microporous layer, features much higher surface area but smaller porosity and is usually constructed of carbon particles bound together with a binder, such as PTFE, which also affords some hydrophobicity.^[21] Moreover, the high surface area microporous layer serves as a substrate for ORR and OER catalyst loading.^[5] Indirect catalyst loading, often via spray-coating, deposits catalyst particles on the outermost surface of the microporous layer only (Figure 1a). Direct catalyst loading techniques, on the other hand, can take advantage of the porosity in the microporous layer to increase the amount of catalyst loading. A gas-phase technique, atomic layer deposition (ALD) can deposit catalyst layers on GDL particles deep within the porosity since it does not require line-of-sight (Figure 1b). This leads to an improvement in the utilization of the catalyst on the GDL. Furthermore, the deep penetration of catalyst material into the substrate can increase the resiliency of the air electrode against electrolyte flooding during prolonged battery cycling, extending the battery's lifetime.^[9]

Often categorized as a special form of chemical vapour deposition (CVD), ALD differs from CVD in that chemical species are active only on a substrate surface, eliminating line-of-sight

[a] M. Labbe, M. P. Clark, Dr. K. Cadien, Dr. D. G. Ivey
Department of Chemical and Materials Engineering
University of Alberta
Edmonton, Alberta, Canada T6G 1H9
E-mail: divey@ualberta.ca

Supporting information for this article is available on the WWW under <https://doi.org/10.1002/batt.202400133>

© 2024 The Authors. *Batteries & Supercaps* published by Wiley-VCH GmbH. This is an open access article under the terms of the Creative Commons Attribution Non-Commercial License, which permits use, distribution and reproduction in any medium, provided the original work is properly cited and is not used for commercial purposes.

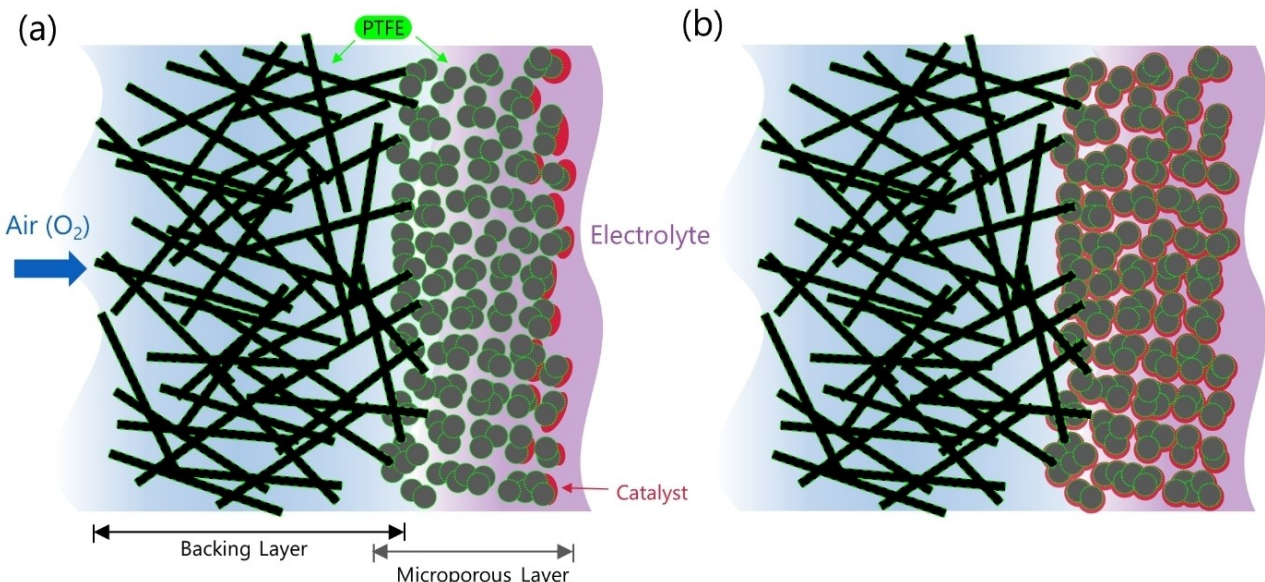


Figure 1. Schematic of the GDL structure and catalyst loading on the air electrode. The green outline around the backing layer and microporous layer particles represents PTFE in the GDL. The catalyst material is shown in red. (a) Representation of an indirect catalyst loading technique, which only coats the outermost surface of the air electrode. (b) Representation of loading catalyst material with ALD, which coats throughout the porosity of the microporous layer.

shortfalls and enabling extremely conformal coatings.^[22] A chemical precursor and co-reactant are separated by inert gas purges to ensure that only surface adsorbed species contribute to material growth.^[23] As a result, ALD coatings are deposited in cycles, with more cycles generally leading to thicker films. A binary ALD process, which often deposits monometallic oxides (e.g., Fe_2O_3), has four steps within one cycle: precursor delivery, inert gas purge, reactant delivery, and inert gas purge.^[23] An ALD supercycle is the combination of two or more binary processes to deposit a multi-element film, such as a bimetallic oxide (e.g., $CoFe_2O_4$).^[24] Within one supercycle, there can be several cycles of each binary ALD process, denoted as subcycles (e.g., 5 cycles of Fe_2O_3 and 5 cycles of CoO). The number of subcycles for each material within a supercycle can be tailored for the desired film chemistry.^[25] Like any ALD process, increasing the total number of supercycles results in increased film thickness.^[22] While the ALD chemistry of transition metal single oxides has been extensively explored,^[26] ALD of bimetallic and trimetallic oxides is not as common place.^[25] In particular, there have been a handful of bimetallic oxides explored in the literature that include either Mn or Fe as components,^[27–33] but to the authors' knowledge, this work is the first reporting Mn–Fe oxide ($MnFe_xO_y$) deposited via ALD.

Several reviews have explored the application of ALD towards energy conversion and storage,^[34–37] citing specific examples towards the more established technologies of Li-ion batteries, fuel cells, and solar water splitting devices. For studies on ZABs in particular, ALD is generally focused on catalyst development at the air electrode. In some cases, ALD is applied to a high surface area substrate but the catalyst itself is applied to the air electrode indirectly.^[38–41] Direct ALD onto the air electrode has been conducted for Co_9S_8 ,^[42] NiS_x ,^[43] and MnO_x catalysts.^[9] For the first two instances, carbon nanotube func-

tional additives were added to air electrode, while the latter case was an ALD coating directly on the as-received GDL material. Herein, an ALD recipe to deposit a bimetallic $MnFe_xO_y$ catalyst directly on the air electrode is developed. The ALD supercycle process builds upon previous work in the research group on the binary depositions of MnO_x and FeO_x which have demonstrated catalytic activity towards ORR and OER, respectively.^[44,45] The optimized supercycle process deposits Fe substituted Mn_3O_4 (denoted as $(Mn,Fe)_3O_4$) and produces a uniform layer of the mixed oxide that encases GDL particles. The electrochemical characteristics of the $MnFe_xO_y$ film are a mix of both MnO_x and FeO_x monometallic oxides and the mixed oxide proves to be a stable bifunctional ZAB catalyst, with over 600 h (1565 cycles) of discharge-charge cycling at 10 mA cm^{-2} .

The innovation of the current study is two-fold. Firstly, based on the research of the authors, the current study is the first report of mixed Mn–Fe oxide in the ALD literature. A supercycle process to deposit mixed Mn–Fe oxides is thoroughly investigated and optimized to maximize bifunctional activity towards ORR and OER. Secondly, this work is the first to apply a mixed transition metal oxide catalyst towards ZAB catalysis using ALD supercycles. Previous reports of ALD for ZAB catalysts use binary ALD processes that deposit only single metal oxides. In this work, a supercycle process to deposit a mixed oxide is developed and applied towards ZAB catalysis. One ALD report in the literature has developed a mixed Fe–Pt catalyst, which was deposited using binary processes and annealing post-deposition, as opposed to direct supercycle deposition performed in this study.^[38] Furthermore, mixed Mn–Fe oxide catalysts are rarely reported in the ZAB literature, which also demonstrates the novelty of the present work. In addition to the innovation of the current study, the cycling

stability of the ALD mixed Mn–Fe oxide catalyst is quite good, with over 600 h (1565 cycles) of stable cycling at 10 mA cm^{-2} .

Experimental

ALD

A hot-walled continuous flow ALD reactor (Kurt J. Lesker Company, ALD 150 L) was used to deposit all ALD films at an operating pressure of ~ 1 Torr using ultra high purity Ar (Linde Canada Inc., 99.999%).^[46] A substrate temperature of 150°C was employed for all depositions, unless otherwise specified. A showerhead design supplied the precursor and reactant lines into the reactor.^[47] The system was also equipped with a 600 W inductively coupled radiofrequency remote plasma system, operating with Ar and either O₂ (O-plasma, Linde Canada Inc., 99.993%) or forming gas (FG-plasma: 5% H₂, balance N₂; Linde Canada Inc.).^[46] The Fe precursor (ethylferrocene, EF, STREM Chemicals, Inc., 98%) and Mn precursor (bis(ethylcyclopentadienyl)manganese, (EtCp)₂Mn, STREM Chemicals, Inc., 98%) were maintained at 80°C , with precursor delivery lines and valves heated to 110 and 100°C , respectively. An ampoule of distilled H₂O, serving as the H₂O reactant, was kept at room temperature ($\sim 22^\circ\text{C}$) with a delivery line and ALD valve at 100°C . FeO_x ALD cycles followed the timing scheme of 0.25/5/1/20/5 (EF dose/Ar purge/pre-plasma O₂ flow/O-plasma/Ar purge), while MnO_x ALD cycles followed a timing scheme of 3/5/20/20/2/30 ((EtCp)₂Mn dose/ampoule charge/Ar purge/FG-plasma/H₂O dose/Ar purge). A saturation study for each binary ALD process on their opposing supercycle surface (e.g., FeO_x deposition on a MnO_x surface) revealed that both of these timing values yielded saturating growth during supercycle depositions (Figures S1 and S2).

For electrochemical characterization of ALD films, carbon paper-based GDL (SIGRACET® 39BB, SGL Carbon) substrates were placed in the ALD reactor with a 60 s O-plasma pretreatment prior to deposition. Film growth was monitored *in situ* using spectroscopic ellipsometry (SE) on a Si(100) witness wafer piece (University Wafers, 525 μm p-type single side polished) placed adjacent to the GDL material in the reactor. The spectrometer (J.A. Woollam Co., Inc., M-2000DI) was directly connected to the ALD reactor and SE results were analyzed in CompleteEase (J.A. Woollam Co., Inc., ver. 4.48) using Tauc Lorentz oscillators to model the ALD films during growth.^[48,49] Previous work has determined that the FeO_x ALD process deposits a homogenous, nano-crystalline phase of Fe₂O₃.^[45] Nevertheless, the ALD process and resulting material deposited through the EF and O-plasma process will be referred to as FeO_x in this work. Previous work on the MnO_x ALD process, on the other hand, could not completely identify the phase(s) present in the deposited material and, thus, the nomenclature of MnO_x employed in that work is utilized here.^[9,44] Furthermore, a 30 min 300°C *ex situ* annealing treatment was investigated for select ALD coated GDL samples, which are referred to as annealed. Samples without an annealing treatment are referred to as unannealed.

Electrochemical Characterization

The half cell setup featured ALD coated GDL as the working electrode, submerged in a 1 M KOH (Fisher Chemical, certified ACS) electrolyte saturated with ultra high purity O₂ (Linde Canada Inc., 99.993%) flowing at 40 standard $\text{cm}^3 \text{ min}^{-1}$. The room temperature ($\sim 22^\circ\text{C}$) electrolyte also contained a platinum coil counter electrode and Hg/HgO reference electrode (0.098 V vs. SHE). A Biologic VSP potentiostat was used to conduct linear sweep voltammetry (LSV) at both ORR and OER potentials. The onset of ORR and OER was measured at a current density of 10 mA cm^{-2} . The full cell setup

featured ALD coated GDL as the air electrode with a 0.5 mm thick strip of as-received Zn foil (McMaster-Carr, 99%) acting as the Zn electrode. The homemade vertical ZAB cell is described elsewhere.^[7,50] Ambient air entered the cell through the GDL without mechanical assistance and the electrolyte was 6 M KOH and 0.25 M ZnO (Fisher Chemical, certified ACS). A Biologic VSP potentiostat was used to conduct galvanostatic discharge and charge tests at $|2|$, $|5|$, $|10|$ and $|20| \text{ mA cm}^{-2}$, with a hold period of 10 min each. Using the values at a current density of $|20| \text{ mA cm}^{-2}$, the efficiency of a candidate catalyst was calculated as the discharge potential divided by the charge potential. Long-term cycling tests employed a similar battery cell to the full cell design but with additional provisions to reduce electrolyte loss.^[51] An Arbin LBT20084 battery cycler was used to conduct galvanostatic cycling at $|10| \text{ mA cm}^{-2}$, with 10 min charge and discharge periods. For the first 200 cycles (100 h), a 5 min rest period was added between charge and discharge. For cycles beyond 200, the rest period was reduced to 1 min.

Individual oxides of MnO_x and FeO_x were deposited on GDL using the binary ALD processes to electrochemically compare with the mixed oxide catalyst. As with previous work,^[45] ALD of FeO_x on GDL was preceded by 10 cycles of MnO_x ALD to protect the carbon substrate. The FeO_x sample was only deposited to a thickness of 10 nm due to its slow growth rate. The MnO_x sample was deposited to a thickness of 40 nm. In addition, a Pt–Ru–C catalyst benchmark comparison was prepared via spray-coating an ink onto GDL substrates with a mass loading of $\sim 1 \text{ mg cm}^{-2}$. The ink was a mixture of a commercial Pt–Ru–C powder (Alfa Aesar; 40 wt% Pt, 20 wt% Ru, balance carbon black), a 60 wt% PTFE dispersion (Chemours Teflon™ PTFE DISP 30), reagent alcohol (Fisher Chemical, histological grade), and H₂O. The FeO_x, MnO_x and Pt–Ru–C samples were also annealed at 300°C for 30 min.

Materials Characterization

Scanning electron microscopy (SEM) imaging and energy dispersive X-ray (EDX) analysis were conducted at 20 kV and a working distance of 15 mm using a TESCAN Vega3 tabletop SEM equipped with an EDX detector. Transmission electron microscopy (TEM) samples were prepared by scraping off the microporous layer of ALD coated GDL, dispersing in reagent alcohol, and drop casting onto carbon coated, Cu TEM grids (Ted Pella, Inc., Prod #01881-F). TEM/scanning TEM (STEM) was conducted at 200 kV using either a Tecnai Osiris TEM/STEM or a JEOL JEM-ARM 200CF TEM/STEM, both equipped with EDX detectors. Selected area diffraction (SAD) patterns were obtained for crystal structure analysis. X-ray photo-electron spectroscopy (XPS) of the ALD films on Si(100) wafers was conducted using a VersaProbe III instrument with monochromatic Al K α (1486.6 eV) radiation. A 60 s Ar sputtering pretreatment was used to remove adventitious carbon. XPS spectra were analyzed in CasaXPS software (version 2.3.19), with Shirley type background subtraction for all spectra,^[52–56] and a GL(30) curve shape for all peak fitting.^[53,55–57]

Results and Discussion

Supercycle Optimization

Due to the self-limiting nature of ALD, no more than one monolayer of material can be deposited per cycle. This affords precise control over the thickness of individual layers used to construct a ternary oxide film. As explained in a review by

Mackus et al., there are two main parameters that can be modified to tailor a supercycle process: the cycle ratio and the bilayer period.^[25] The cycle ratio describes the compositional mix of the two individual ALD processes, while the bilayer period characterises the thickness of each layer used in the supercycle. In this work, the nomenclature adopted describes the number of MnO_x ALD cycles deposited followed by the number of FeO_x ALD cycles deposited, in one supercycle. For example, the sample labelled 30:10 indicates that 30 MnO_x ALD cycles were deposited, followed by 10 FeO_x ALD cycles, and this was then repeated until the desired thickness was reached (Figure 2). Following the nomenclature presented by Mackus et al., 30:10 employs a cycle ratio of $(30/40) = 0.75$ for MnO_x and $(10/40) = 0.25$ for FeO_x , with a bilayer period of $(30+10) = 40$. During supercycle optimization, ALD films were deposited to a total thickness of approximately 10 nm to be comparable with the thickness of the binary ALD FeO_x films developed previously.^[45] However, due to the digital nature of supercycles, not all films were exactly 10 nm; the exact number of supercycles employed and the resulting thickness of each sample are reported in Table S1.

In a similar manner to other reports of ternary oxide catalysts for ZABs,^[8] the composition of deposited films is systematically manipulated to optimize the catalytic performance. To evaluate bifunctional catalytic performance, two common electrochemical techniques employed in ZAB testing were used. Half cell tests submerge the ALD coated GDL into an electrochemical cell to study the oxygen half cell reactions (ORR and OER). Full cell tests employ the ALD coated GDL as the air electrode in a homemade ZAB cell, studying the rate performance of the air electrode. All samples were investigated via the half cell configuration, while only those showing promising results were examined further in the full cell configuration. Aside from the elemental composition of the ALD films, the application of an annealing treatment was also studied during the optimization process. Previous reports for ZAB catalysts have also explored an annealing treatment, with overall mixed results.^[8,44,58,59] Complete performance metrics (extracted from half cell and full cell results) for all samples explored in this work are summarized in Table S2.

Casting a Wide Net

As an initial survey of cycle ratios and bilayer thicknesses, three different supercycle schemes were tested: 1:10, 5:30, and 10:20. In this way, the FeO_x cycle ratio varies from 0.91 to 0.67 and the bilayer period varies from 11 to 35, casting a wide net to uncover the optimal supercycle scheme. Figure 3a shows the half cell performance of these films, in both unannealed and annealed conditions. The sample with the highest MnO_x cycle ratio (10:20) exhibits the lowest half cell ORR overpotential (η). This is not surprising considering MnO_x is the ORR-active species in the supercycle. Furthermore, annealing improves the half cell ORR onset for the MnO_x -rich sample, in-line with the results from other studies.^[44] Conversely, the sample with the highest FeO_x cycle ratio (1:10) provides the best half cell OER onset since FeO_x is the OER-active species. Thus, overall, larger proportions of MnO_x provide better ORR performance, but at the expense of lower OER performance due to the reduced proportion of FeO_x . Quantifying the half cell results by calculating the voltage gap between charge and discharge (Table S2), the annealed 10:20 sample provides the best bifunctional performance in half cell. The full cell results in Figure 3b do not vary as much among samples compared with the half cell results, but annealing consistently improves discharge potentials at the expense of increasing the charge potential. Nevertheless, annealing typically results in an increased overall bifunctional efficiency. Based on the combined results of half cell and full cell testing, the 10:20 sample was considered for further optimization, in both unannealed and annealed states.

Cycle Ratio Optimization

To further optimize the composition of the MnFe_xO_y catalyst, the cycle ratio of MnO_x was varied from 0.8 to 0.2, with a bilayer period restricted to factors of 10 (like that exhibited by the 10:20 sample). As shown in Figure 3c, generally, the half cell OER onset is reduced as the MnO_x cycle ratio is reduced (and the FeO_x cycle ratio is increased). At the same time, the half cell

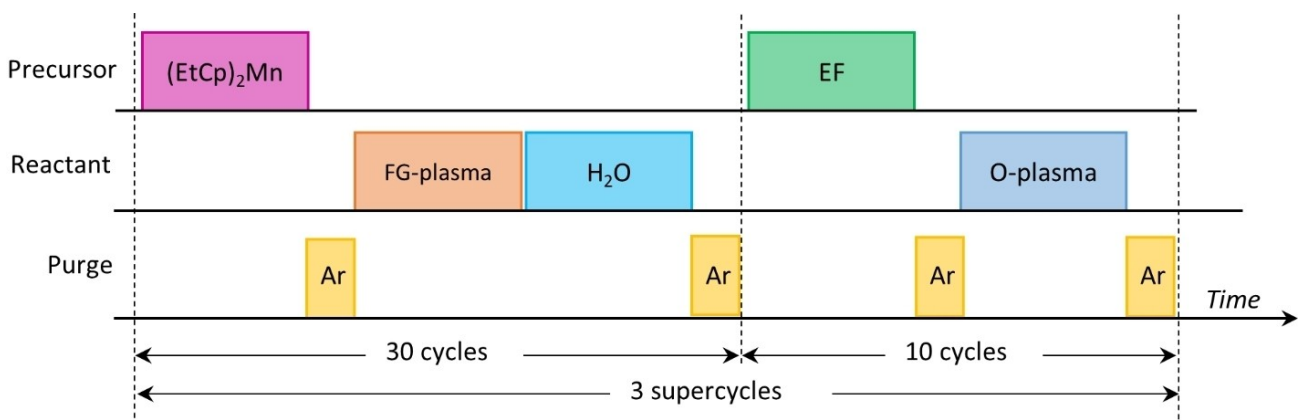


Figure 2. Schematic of the atomic layer deposition (ALD) supercycle process for a 10 nm thick 30:10 MnFe_xO_y sample.

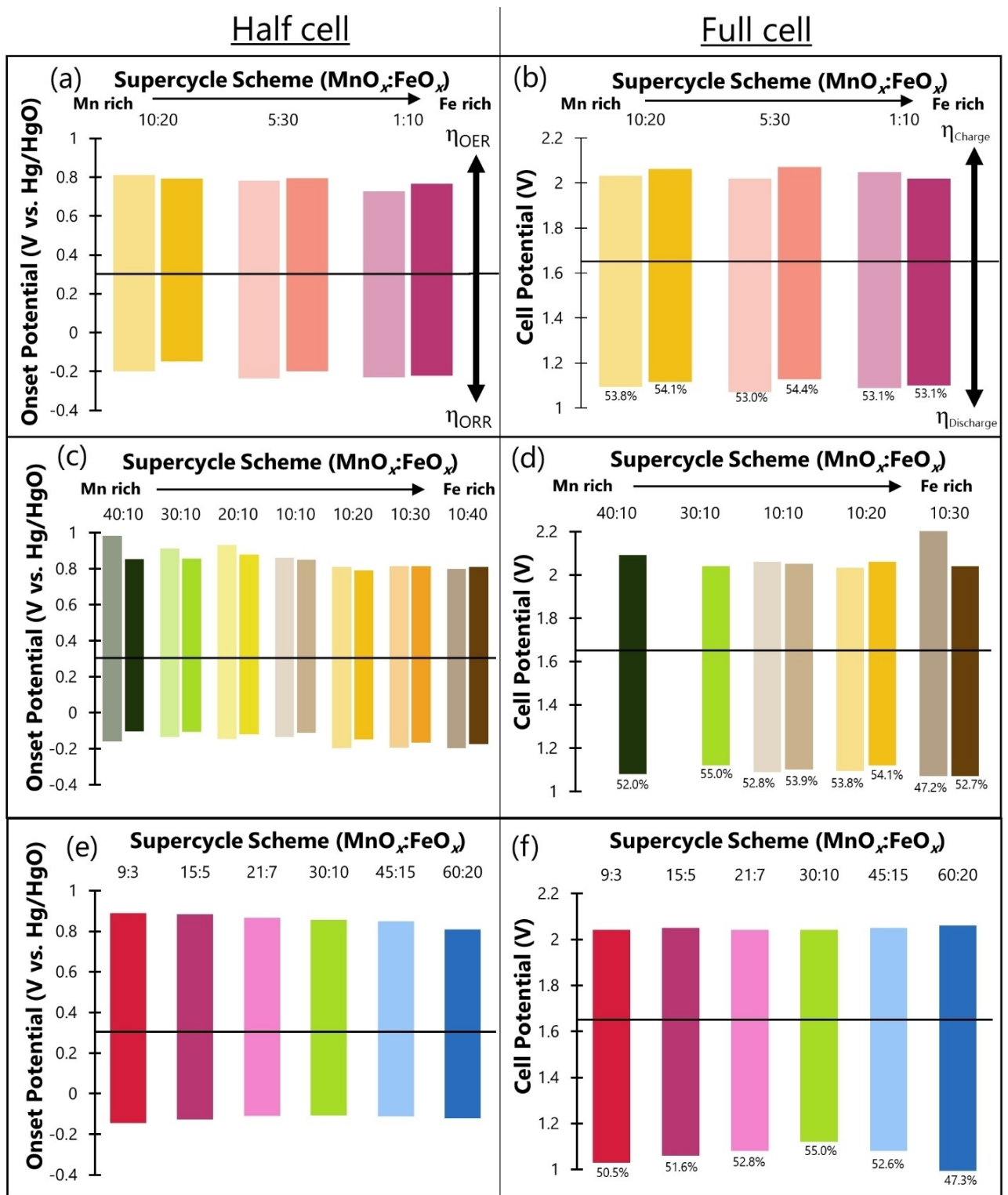


Figure 3. Stages of optimization for the MnFe_3O_4 supercycle recipe. (a, b) An initial survey of compositions, (c, d) optimization of the cycle ratio, and (e, f) optimization of the bilayer thickness. Boxes a, c, and e represent half cell performance, while boxes b, d, and f are full cell results. Lighter shade bars (on the left of each label) indicate an unannealed sample, while dark shaded bars (those on the right) represent annealed samples. In (e) and (f), only annealed sample results are presented.

ORR onset is increased as the MnO_x cycle ratio is reduced. These effects are similar to the trend observed in Figure 3a, where more MnO_x content translates into improved ORR performance

at the expense of OER performance. Referring to the voltage gap data (Table S2), the annealed 10:20 sample continues to provide the best bifunctional half cell performance. Not all

samples were subsequently studied in full cell and, based on the onset potentials during half cell, the unannealed and annealed 20:10 and 10:40 samples were excluded from further analysis, in addition to the unannealed 40:10 and 30:10 samples. The remaining samples were studied in full cell and the results are shown in Figure 3d. The annealed 30:10 sample yields the highest bifunctional efficiency at 55.0% at 20 mA cm^{-2} . Therefore, this sample is the best MnFe_xO_y catalyst thus far and was considered for further optimization. Note that the annealed 10:20 sample is a close second at 54.1% bifunctional efficiency. For almost all the samples in Figures 3c and 3d, annealing results in improved bifunctional efficiency and, therefore, all samples explored hereafter were subjected to annealing.

Bilayer Thickness Optimization

The 30:10 sample results in a MnO_x cycle ratio of 0.75 and the ratio was kept constant as the bilayer thickness was modified. Bilayer periods ranging from 11 to 80 were investigated and the electrochemical results of the annealed samples are shown in Figures 3e and 3f. Surveying the half cell results (Figure 3e), the annealed 60:20 sample provides the best overall bifunctional performance. This is mainly due to an improved OER onset, however, as the ORR onset is less sensitive to the bilayer period. The full cell results (Figure 3f) display the opposite effect. The discharge potential varies greatly with bilayer period, whereas the charging potential is relatively constant. In this case, the 60:20 sample is the worst bifunctional catalyst. While it was intended that all samples in Figures 3e and 3f have similar thicknesses, the 60:20 sample is 15–25% thicker than the other samples (Table S1). A 60:20 supercycle, with the largest bilayer period of 80, does not allow for precise thickness adjustments: two supercycles results in a 14 nm thick film, while only one supercycle yields a 7 nm film. The larger thickness for the 60:20 sample results in a lower half cell OER onset potential, a phenomenon that has also been observed when comparing 10 and 40 nm thick ALD MnO_x samples. The bifunctional efficiency of full cell testing is a more important criterion, since full cell testing better represents actual ZAB performance. Thus, the annealed 30:10 sample is considered the best MnFe_xO_y supercycle composition. There is also a trend in the discharge potentials of Figure 3f based on the bilayer period. The 30:10 sample has a bilayer period of 40, whereas the 21:7 and 45:15 samples have bilayer periods of 28 and 60, respectively. With similar amounts of deviation from the optimal bilayer period of 40, both the 21:7 and 45:15 samples have reduced discharge potentials. This trend continues for the 9:3, 15:5, and 60:20 samples, which deviate even further from a bilayer period of 40 and, thus, have even more inferior discharge potentials. This trend reaffirms that 30:10, with a bilayer period of 40, is the best MnFe_xO_y ALD supercycle composition.

Increasing Overall Thickness

Samples discussed thus far have been deposited to a thickness of roughly 10 nm in order to be comparable with the thickness of the FeO_x sample (which itself is limited to only 10 nm due to a low ALD growth rate).^[45] It is anticipated that improvements in catalytic performance can be achieved by depositing thicker films. As such, the best supercycle composition of 30:10 was deposited to a total thickness of 20, 30, and 40 nm. The half cell results in Figure S3a demonstrate that increasing thickness improves the OER onset. These results also support the explanation as to why the 60:20 sample yields the best half cell OER performance when manipulating the bilayer period. Not surprisingly, the thickest film also provides the best overall bifunctional half cell performance. However, full cell results in Figure S3b are less straight-forward. An increase in thickness does provide a benefit for the discharge potential, but the charging potential is more scattered, without any apparent trend. Nevertheless, based on bifunctional efficiency values in Figure S3b, the 40 nm thick 30:10 sample is still regarded as the best catalyst explored so far. The estimated mass loading on GDL for this sample is $50 \mu\text{g cm}^{-2}$. Hereafter, unless otherwise specified, the nomenclature MnFe_xO_y will refer to the annealed 40 nm thick 30:10 MnFe_xO_y ALD sample.

Materials Characterization of MnFe_xO_y

SEM

Low magnification SEM images of the unannealed and annealed MnFe_xO_y coating on GDL (Figures S4a–b and S5a–b) are essentially identical, revealing no apparent microscopic morphological changes after the annealing treatment. EDX spectra from both samples (Figures S4c and S5c) indicate a Mn/Fe atomic ratio of roughly 3, as anticipated by the 30:10 supercycle process. Elemental mapping (Figures S4d–g and S5d–g) shows complete surface coverage with Mn, Fe, and O species. Minor Mn and Fe enrichment occurs at edge features of the microporous surface. For the most part, edge effects from the electron beam interaction volume can account for this phenomenon.^[60] However, it is also possible that the cavities surrounding the edge features in the microporous layer allow for increased diffusion of precursor species during ALD, leading to an increased amount of deposition on edge surfaces.^[61]

TEM/STEM

TEM/STEM examination of the MnFe_xO_y coating on GDL, in the unannealed state, is presented in Figure 4. The GDL material featured in the STEM bright field (BF) images (Figures 4a and 4b) displays a dark border encasing each carbon particle, representing the higher atomic number MnFe_xO_y coating. A STEM high angle annular dark field (HAADF) image from another region (Figure 4c) displays an ALD coating thickness of ~25 nm. *In situ* SE during ALD growth indicated a film thickness

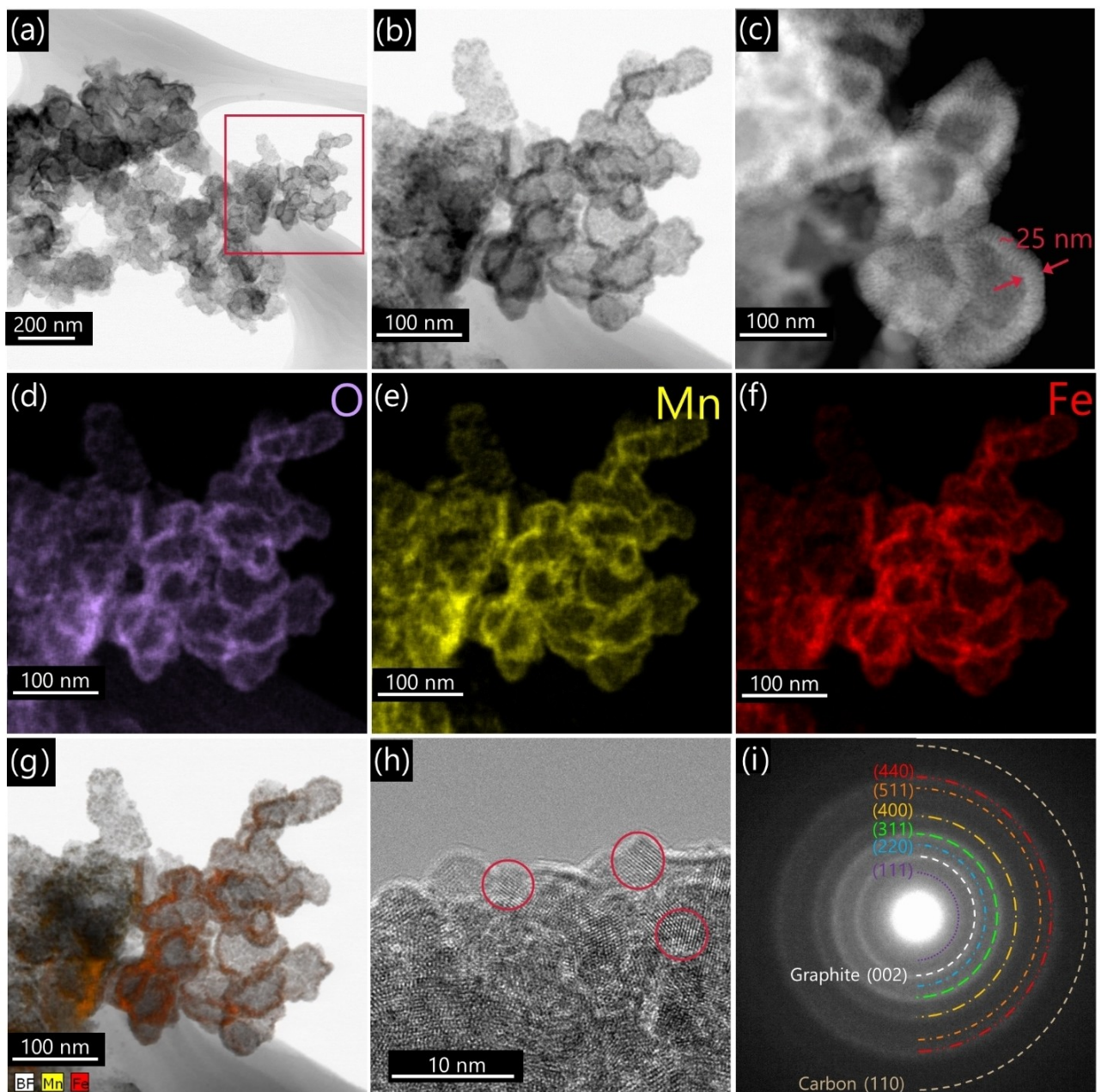


Figure 4. TEM/STEM characterization of an unannealed MnFeO_x coating on GDL. (a) STEM BF image, (b) magnified image of the indicated area in (a). (c) Higher magnification STEM HAADF image from another region. EDX mapping (from region (b)) showing (d) O, (e) Mn, and (f) Fe. (g) Overlapping maps of Fe and Mn on the BF image. (h) HRTEM image, with red circles identifying a few individual grains. (i) SAD pattern from the region shown in (a).

of 40 nm. This discrepancy in thickness is attributed to sampling errors during preparation of the TEM sample. ALD coated particles of the air electrode are scraped off and affixed to a TEM grid, but the location of these particles can be from deep within the air electrode porosity, where there is lower ALD coverage.^[9,44,45] The outer-most surface particles of the air electrode likely contain a 40 nm thick coating, but it is difficult to prepare a TEM sample of only these particles. EDX maps (Figure 4d-g) reveal overlapping signals of O, Mn and Fe. There are no discrete layers of Mn and Fe, but rather a homogenous mixture, demonstrating that the ALD supercycle process produces a mixed oxide and not separate films of each oxide.

The EDX spectrum (Figure S6a) shows a Mn/Fe atomic ratio of ~1.5, which is lower than that from SEM analysis (Figure S4c). This may be a sampling phenomenon, as the volume of material analyzed using EDX spectroscopy in the STEM is significantly smaller than that in the SEM. As such, EDX analysis in the SEM is less localized and more representative of the overall composition. Based on the high resolution TEM (HRTEM) image in Figure 4h, the coating is nanocrystalline; the red circles in Figure 4h highlight crystalline grains. The nanocrystallinity is also reflected in the SAD pattern (Figure 4i) taken from the overall region shown in Figure 4a. There are several diffuse rings which can be indexed to several possible oxides of Mn

and Fe. The best fit is to Fe_3O_4 , Mn_3O_4 , and MnFe_2O_4 , which are all isostructural (cubic spinel); a comparison of d-spacings is provided in Table S3. The relatively strong diffraction ring at a d-spacing of 0.354 nm is attributed to graphitic GDL, while the diffraction rings at 0.125 nm and 0.211 nm can be matched to the carbon TEM grid as well as the ALD film (Figure S7 and Table S3).^[9] Figure S8 shows TEM dark field (DF) images obtained from part of the (311) and (400) rings in Figure 4i. The bright spots in the images correspond to individual nanocrystals of the MnFeO_x film.

STEM analysis of the MnFeO_x coating on GDL in the annealed condition reveals that the ALD coating undergoes a

slight nanoscopic morphology change upon annealing. Whereas before the ALD film was smooth and uniform, after annealing the coating breaks up into more discrete nanoparticles, as evident in the STEM BF images (Figures 5a and 5b). This likely increases the effective area for catalysis, resulting in the electrochemical improvements noted earlier for the annealed samples during supercycle optimization. The driving force for this phenomenon is unclear. One possibility is that there is residual stress in the ALD coating and annealing enables redistribution of atoms into nanoparticles to reduce interfacial stress, not unlike the Stranski-Krastanov growth model of thin films.^[62] Another possibility is that the slight migration of atoms

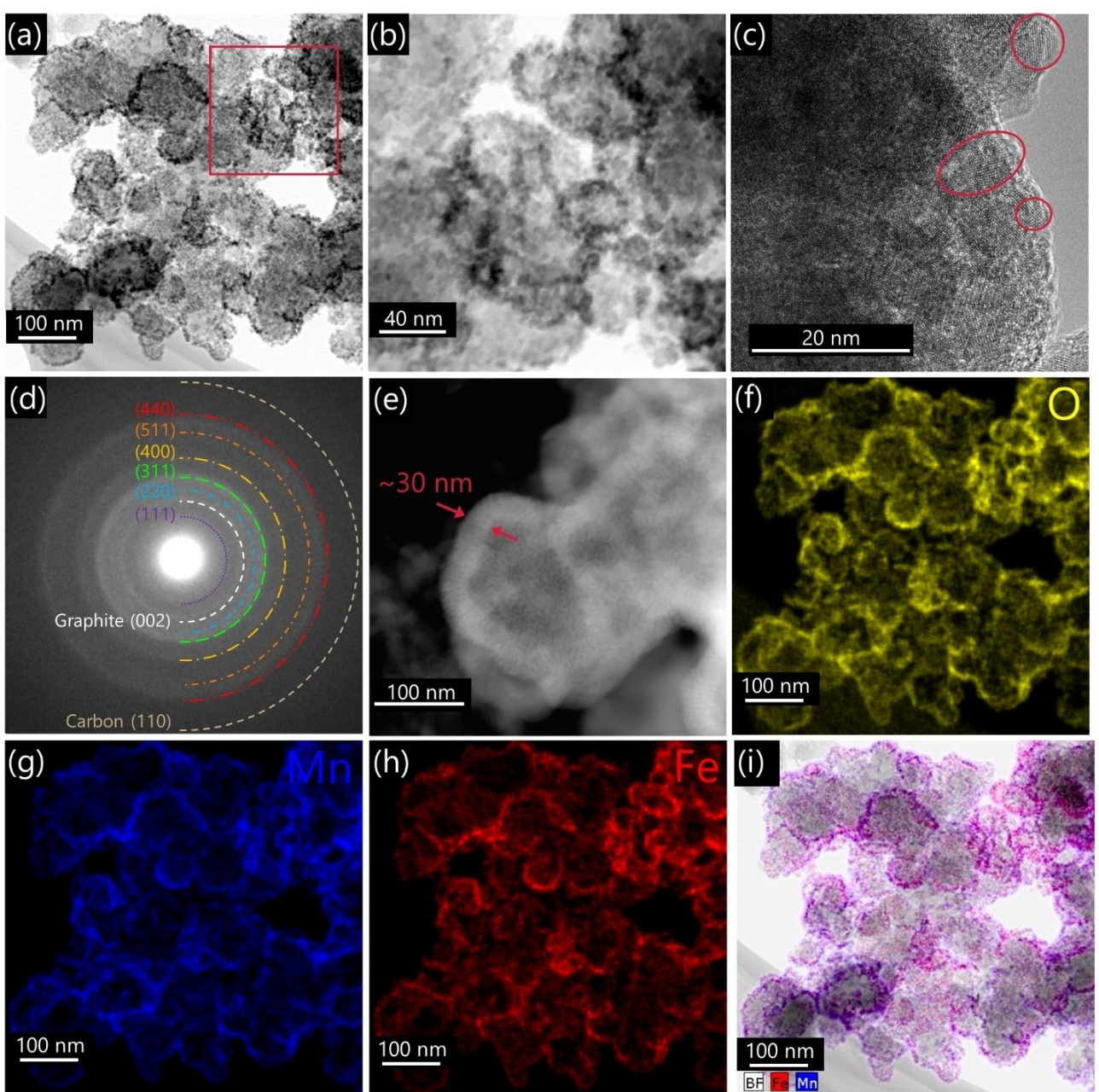


Figure 5. TEM/STEM characterization of an annealed MnFeO_x coating on GDL. (a) STEM BF image, (b) magnified STEM BF image of the indicated area in (a). (c) HRTEM image, with red circles identifying a few individual grains. (d) SAD pattern from the region in (a). (e) High magnification STEM HAADF image from another region. EDX mapping (from region (a)) showing (f) O, (g) Mn, and (h) Fe. (i) Overlapping maps of Fe and Mn on the BF image.

into discrete nanoparticles, enabled by annealing, leads to a more thermodynamically stable arrangement of discrete crystalline regions. However, the HRTEM image (Figure 5c) and electron diffraction pattern (Figure 5d) indicate no noticeable improvement in the crystallinity of the coating after annealing. The SAD pattern of the annealed sample (Figure 5d) is very similar to the unannealed sample (Figure 4i) and can be indexed to the same crystal structures (Table S3). Figure 5e shows a DF image from a different region where the ALD coating thickness is ~30 nm. EDX mapping (Figure 5f-i) again shows overlapping signals of Mn, Fe, and O, without any evidence of elemental segregation after annealing. The STEM EDX spectrum (Figure S6b) indicates a Mn/Fe atomic ratio of 3.1, which is in line with the 30:10 ALD supercycle used to produce the film and agrees with the SEM EDX results (Figure S5c).

XPS

XPS was conducted on both the unannealed and annealed MnFeO_x deposits to further study the chemical state. The Si substrate samples were selected for analysis to obtain better XPS spectra. Figure 6a shows the overall survey spectra for the unannealed and annealed samples. Quantitative analysis was carried out for the regions highlighted in Figure 6a and is shown in the pie charts in Figure 6b. The unannealed spectrum features a small contribution from F and N, while both spectra exhibit significant Mn, Fe and O peaks. An Ar peak is identified in both spectra as a result of the sputter clean performed prior to XPS analysis. The N signal in the unannealed sample likely results from the FG-plasma used during MnO_x ALD cycles and, similar to other reports, is reduced or eliminated entirely upon annealing.^[9,44] The F peak in the unannealed sample is the result of volatile F species that deposit on the Si substrate during ALD growth. These volatile F species originate from plasma treatment of the GDL substrate (which contains PTFE) that is also present in the ALD reactor. Like N, the F contribution is removed with annealing.

The C 1s spectra (Figure S9) feature deconvolution results in line with previous investigations on carbon-based GDL substrates,^[44] and the main peak was set to 284.8 eV to calibrate the rest of the XPS results.^[44,53,63] Detailed deconvolution results for all XPS spectra are tabulated in Table S4. For the O 1s spectra (Figure 6c), the main peak (shown in blue) results from lattice oxygen and was fit to 529.5 and 529.6 eV for the unannealed and annealed sample, respectively.^[54,63–65] Contributions from hydroxyl species (shown in orange) were fit to the shoulders featured at 531.2 and 531.0 eV for the unannealed and annealed samples, respectively.^[8,54,63–66] The full width at half maximum of these peaks was constrained to values found in the literature.^[63,64] The annealed sample has a smaller component of hydroxyl species in the O 1s spectrum, which is similar to the annealed C 1s spectrum (Figure S9).^[8] Lastly, a peak at 531.8 eV was fit to both spectra (shown in green) to account for the ester and/or carbonyl contributions identified in the C 1s spectra.^[44,63,67,68]

The Fe 2p spectra, shown in Figure 6d, exhibit separate 2p_{3/2} and 2p_{1/2} peaks because of spin-orbit coupling.^[69] Multiplet splitting of the 2p_{3/2} curve was fit using both Fe²⁺ and Fe³⁺ contributions (shown in orange and blue, respectively),^[53,70] and the relative area of the two oxidation states resulted in a calculated overall oxidation state for Fe of 2.6 for both the unannealed and annealed samples.^[8,71] This agrees with the electron diffraction patterns which were indexed to a spinel structure (e.g., Fe₃O₄), which has an oxidation state of 2.67. Furthermore, the position of the Fe 2p_{1/2} peak for the unannealed and annealed samples (shown in yellow) was fit to 724.3 and 723.8 eV, respectively, which both align with Fe₃O₄.^[7,72] A small satellite feature around 718.0 eV (shown in green) was identified in the unannealed spectrum. This satellite feature is normally absent in Fe₃O₄ spectra and thus indicates the existence of a small amount of some other Fe structure in the unannealed sample.^[72,73] This may be Fe₂O₃, as previous work by the authors demonstrated that the binary ALD FeO_x process deposits as Fe₂O₃.^[45] Upon annealing, Fe and O species are able to fully diffuse into the mixed Mn–Fe oxide spinel structure, eliminating the satellite feature in the Fe 2p spectrum.

The Mn 2p spectra, shown in Figure 6e, also display spin-orbit coupling. Multiplet splitting was fit using Mn²⁺, Mn³⁺, and Mn⁴⁺ contributions (shown in blue, orange, and yellow, respectively),^[8,53,74] and the overall oxidation state was calculated to be 2.7 and 2.6 for the unannealed and annealed samples, respectively. This result is in agreement with the electron diffraction results, where the SAD patterns were indexed to a mixed Mn–Fe oxide spinel structure, designated as (Mn,Fe)₃O₄. On the other hand, the position of the overall Mn 2p_{3/2} peak lies at 640.6 and 640.3 eV for the unannealed and annealed samples, respectively. Comparison of this peak position with the literature suggests that Mn in MnFeO_x exists as MnO (i.e., a Mn²⁺ oxidation state).^[75–77] As well, the overall shape of the Mn 2p spectra, with pronounced satellite features for both 2p_{3/2} and 2p_{1/2}, bares a striking resemblance to published spectra for MnO.^[78] Another means of determining the oxidation state for Mn is by measuring the amount of peak splitting that occurs for the Mn 3 s spectrum (Figure 6f).^[8,44] For the unannealed sample, two peaks can be fit at 88.59 and 82.42 eV (orange and blue, respectively). For the annealed sample, these peaks are fit to 88.63 and 82.38 eV (Table S4). The result is peak splitting of 6.17 and 6.25 eV for the unannealed and annealed samples, respectively (Figure 6f). Literature values for Mn 3 s peak splitting are generally lower than 6.0 eV, with an anticipated peak splitting for Mn₃O₄ anywhere from 5.5 to 5.8 eV.^[54,55,76] Mn 3 s peak splitting above 6 eV indicates a Mn²⁺ oxidation state, as reported for MnO reference samples.^[55,75,79–82] Yet another method of estimating the oxidation state of Mn is to measure the separation between the Mn 2p_{1/2} main peak and its satellite feature ($\Delta 2p_{1/2}$).^[9] For the current work, $\Delta 2p_{1/2}$ values of 6.06 and 6.05 eV are measured for the unannealed and annealed samples, respectively (Figure 6e). This value also corroborates a Mn²⁺ oxidation state when compared with literature values.^[55]

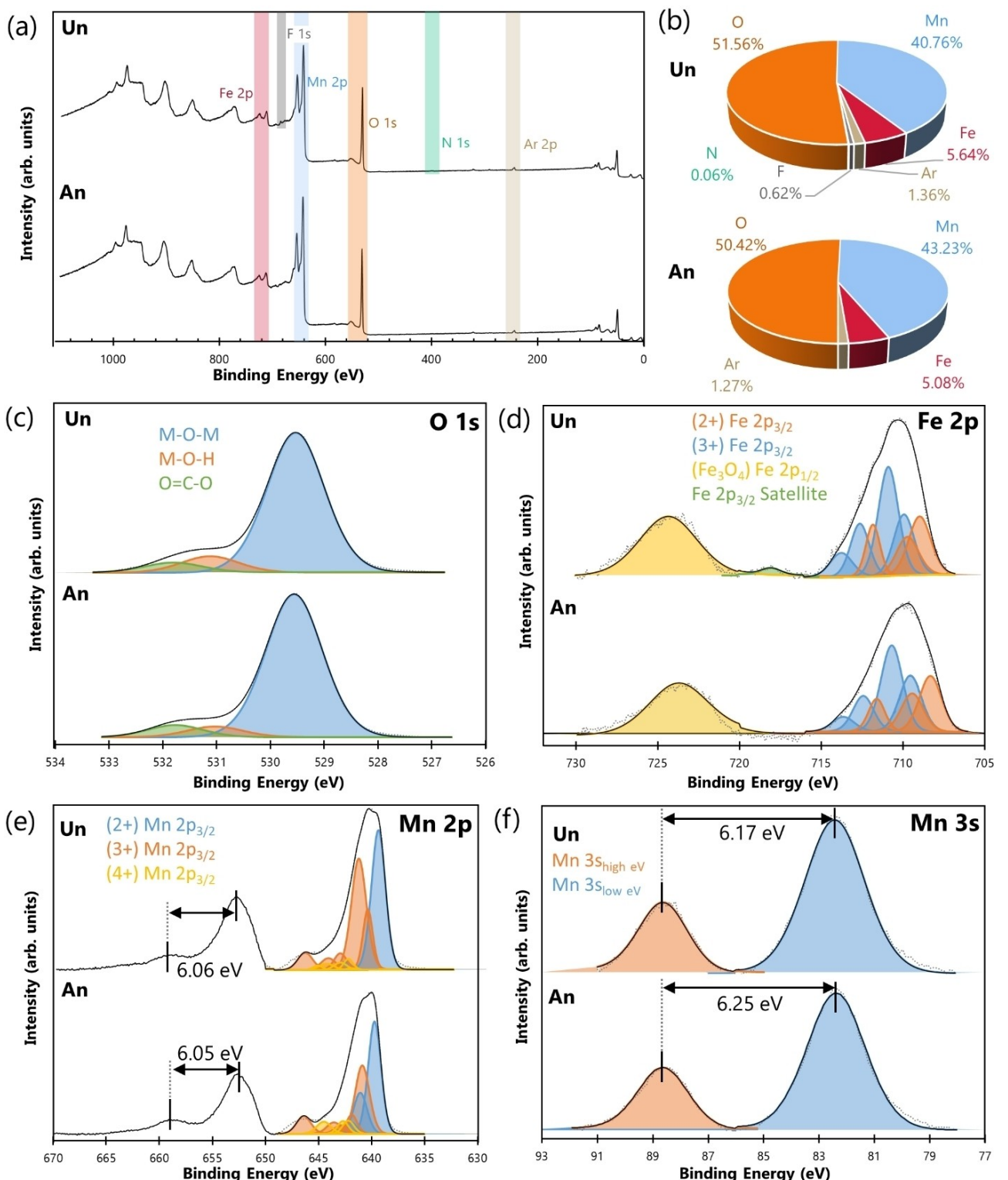


Figure 6. XPS results for unannealed (Un) and annealed (An) MnFeO_x on Si. (a) Survey spectra, (b) quantitative analysis from the survey spectra, and (c-f) deconvolution of the O 1s, Fe 2p, Mn 2p, and Mn 3 s spectra.

Quantitative analysis of the unannealed and annealed survey spectra (Figure 6b) yields a Mn/Fe atomic ratio of 7.2 and 8.5, respectively. These values are well above ~ 3 , the value determined from SEM and STEM and anticipated by the 30:10

supercycle mix. Based on the thermodynamic potentials of Mn and Fe oxidation,^[83] there is a greater driving force for the creation of MnO_x as opposed to FeO_x . As such, it is likely that the surface layer examined by XPS was enriched by Mn species

preferentially oxidizing at the air interface. Furthermore, both XPS samples were exposed to 60 s of Ar sputtering to remove adventitious carbon. This Ar sputtering can also preferentially sputter oxygen species, inadvertently reducing the chemical species at the surface of the material.^[84,85] Therefore, the Mn XPS analysis, which indicates an oxidation state of Mn^{2+} , does not represent the bulk oxidation state of the mixed Mn–Fe oxide. The Fe XPS analysis, on the other hand, which indicates a mixed oxidation state of $Fe^{2.6+}$ and supports the existence of Fe_3O_4 , agrees with the electron diffraction results which can be matched to several different spinels of Mn, Fe, and O. Taken together with the Mn/Fe atomic ratios from EDX analysis, the crystal structure of the mixed Mn–Fe oxide is most likely a mixed spinel oxide of the type $(Mn_xFe_{3-x})O_4$, where Mn and Fe have mixed valences of 2+ and 3+ and the overall ratio of Mn:Fe is ~3.

ZAB Application of $MnFeO_x$

Electrocatalytic Activity

Figure 7 displays electrochemical performance values of the $MnFeO_x$ ALD coating on GDL towards the oxygen reactions involved at the air electrode in ZABs. Also featured in Figure 7 are several different benchmark catalysts to compare the performance of $MnFeO_x$. All samples were exposed to a 30 min 300 °C *ex situ* annealing treatment, except for bare GDL (a substrate sample without catalyst). When the mixed oxide ($MnFeO_x$) catalyst is compared with its monometallic constituents of MnO_x and FeO_x , both also deposited via ALD, the advantages of the mixed oxide become apparent. In half cell testing (Figure 7a), the poor OER performance of MnO_x is augmented by the addition of FeO_x and the resulting mixed

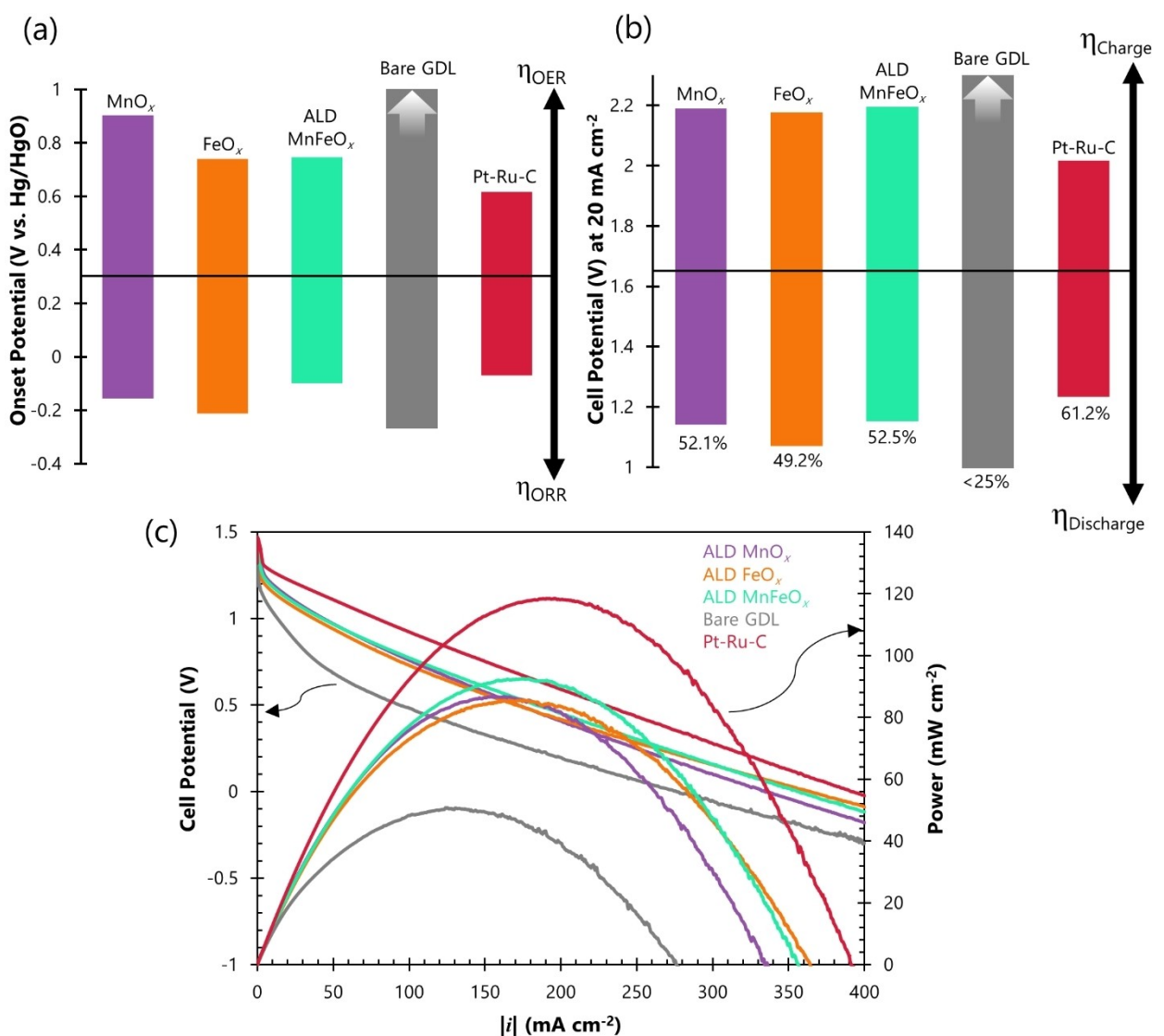


Figure 7. ZAB test results for ALD deposited MnO_x , FeO_x , and $MnFeO_x$, compared with bare GDL and a benchmark Pt–Ru–C catalyst. (a) Half cell onset potentials at $|10 \text{ mA cm}^{-2}|$. (b) Full cell discharge and charge operating voltages and bifunctional efficiencies at $|20 \text{ mA cm}^{-2}|$. The OER/charge performance of bare GDL in half cell/full cell is very poor and the values extend beyond the plot, as represented by arrows. (c) Full cell discharge polarization (left axis) and power density (right axis) curves.

film has an OER onset similar to that of FeO_x . The good ORR performance of MnO_x is not only retained, but actually improved when mixed with FeO_x and, therefore, the mixed oxide has an overall lower voltage gap than either monometallic oxide film. Full cell testing (Figure 7b) reveals similar charge potentials for both MnO_x and FeO_x and, thus, the charge potential of the mixed MnFeO_x film is also similar. Like the half cell results, the full cell discharge performance of the mixed oxide catalyst is slightly superior to MnO_x and so, among the three catalysts, the overall bifunctional efficiency of MnFeO_x is the highest at 52.5% at 20 mA cm^{-2} . Lastly, discharge polarization and power curves were obtained from full cell ZABs constructed with each catalyst (Figure 7c). The peak power delivered by MnO_x and FeO_x is almost the same at around 86 mW cm^{-2} , while the mixed oxide can deliver over 92 mW cm^{-2} of power, which is an improvement over the monometallic oxides. The mixed Mn–Fe oxide outperforms monometallic MnO_x for both ORR and OER due to several possible effects. Firstly, the electronic conductivity of FeO_x is higher than MnO_x and, thus, the mixed oxide has an increased electronic conductivity compared with MnO_x ,^[86] leading to improvements in the overall electron transfer process.^[87] Secondly, the addition of Fe to MnO_x enables a cubic crystal structure (revealed by SAD) and a reduction of Jahn-Teller distortion in the crystal structure.^[88] In other Mn-based mixed oxides, a reduction in Jahn-Teller distortion and the transformation from a tetragonal to cubic crystal structure led to improvements in both ORR and OER performance.^[89–91] Lastly, the addition of other transition metal elements to MnO_x modifies the oxidation state of Mn and alters the electronic structure of the oxide, resulting in improvements to both ORR and OER kinetics.^[19,92–95]

As another comparison, Figure 7 also shows the electrochemical performance of a bare GDL sample and a spray-coated commercial Pt–Ru–C catalyst. The half cell onset potentials featured in Figure 7a show that ALD prepared MnFeO_x is inferior to the commercial Pt–Ru–C catalyst, although the ORR onsets are close at -0.10 V and -0.07 V , respectively, and complete half cell curves (Figure S10) show that, at higher OER potentials, ALD MnFeO_x is similar to Pt–Ru–C in terms of deliverable current density. The bare GDL substrate shows negligible OER activity but not an insignificant amount of ORR activity. The high surface area carbon structure featured in GDL has been reported to provide some inherent ORR activity.^[1] When examined in full cell (Figure 7b), the bare GDL substrate is extremely ineffective at catalyzing either the discharge or charge reactions, resulting in an overall bifunctional efficiency of less than 25% at a current density of 20 mA cm^{-2} . In fact, the charge potential is beyond the scale of Figure 7b and the complete full cell figure (Figure S11) shows that bare GDL reaches the cut-off voltage of 3.5 V at 20 mA cm^{-2} . As with half cell results in Figure 7a, full cell values in Figure 7b show that Pt–Ru–C is a better ZAB catalyst than the ALD MnFeO_x film, boasting a bifunctional efficiency of 61.2% at 20 mA cm^{-2} compared against only 52.5% efficiency for the ALD film. Nevertheless, compared with other bimetallic and bimetallic oxides catalysts in the ZAB literature, the ALD MnFeO_x catalyst

in this work is quite competitive (Table S5). For example, the complex hydrothermal and pyrolysis synthesis method for creating spinel MnFe_2O_4 /metallic Fe hybrid nanoparticles encapsulated in N-doped mesoporous hollow carbon nanospheres (Fe/Mn–N–C), as reported by Wu et al.,^[20] provides a bifunctional efficiency of 55.6% but at only 8 mA cm^{-2} . In comparison, the current ALD MnFeO_x catalyst delivers 52.5% efficiency at a greater current density of 20 mA cm^{-2} . Another catalyst, an Fe-doped MnO_2 catalyst developed by Mathur and Halder,^[19] provides only 30.2% bifunctional efficiency at 25 mA cm^{-2} .

The polarization and power curves of Figure 7c indicate a peak power density of 119 mW cm^{-2} for Pt–Ru–C and only 51 mW cm^{-2} for bare GDL. Compared with the peak power density of 92 mW cm^{-2} for ALD MnFeO_x , Pt–Ru–C is a better ZAB catalyst than ALD MnFeO_x , prior to cycling. While the electrochemical characterization tests demonstrate that Pt–Ru–C is more catalytically active for ZABs than ALD MnFeO_x , long duration cycling tests (presented in the next section) show the benefit of ALD, which distributes the catalyst material within the porous GDL. Prolonged ZAB cycling can lead to electrolyte flooding into the air electrode, where the reaction sites for the oxygen reactions are shifted to regions deeper within the air electrode. If catalyst material is only deposited on the outermost surface of the electrode, then flooding results in a loss of catalytic reaction sites and a degradation in efficiency. For catalyst preparation techniques that can deposit material deep into the porosity of the air electrode, such as ALD, the migration of oxygen reaction sites during flooding does not necessarily result in the loss of catalytic reaction sites and the improved battery efficiency from the catalyst can be maintained.^[7,9]

Cycling Stability

Practical application of ZABs requires at least several hundred cycles of charge and discharge and, as such, candidate catalysts should be exposed to long-term cycling tests.^[1,4] Figure 8a shows overlapping cycling curves for bare GDL, Pt–Ru–C, and ALD MnFeO_x when cycled at 10 mA cm^{-2} . Individual cycling plots for these catalysts, as well as the other catalysts featured in Figure 7, are included in Figure S12. The bifunctional efficiencies of bare GDL, Pt–Ru–C, and MnFeO_x at various intervals throughout the cycling test are displayed in Figure 8b; the bifunctional efficiencies of the remaining catalysts are included in Table S6. At the beginning of cycling, Pt–Ru–C demonstrates the lowest charge potential and highest discharge potential of all catalysts explored, resulting in the highest bifunctional efficiency of 61.9% at 10 mA cm^{-2} . However, the discharge potential and, especially, the charge potential of the Pt–Ru–C catalyst quickly deviates towards inferior values, resulting in a low bifunctional efficiency of 44.9% at 60 h of 10 mA cm^{-2} cycling. Some recovery in the charging potential is observed around 70 h , but nevertheless, the bifunctional efficiency of Pt–Ru–C remains at 45.3% or below for the remaining 530 h of cycling. The instantaneous improvement in charging potential for Pt–Ru–C at 70 h is likely

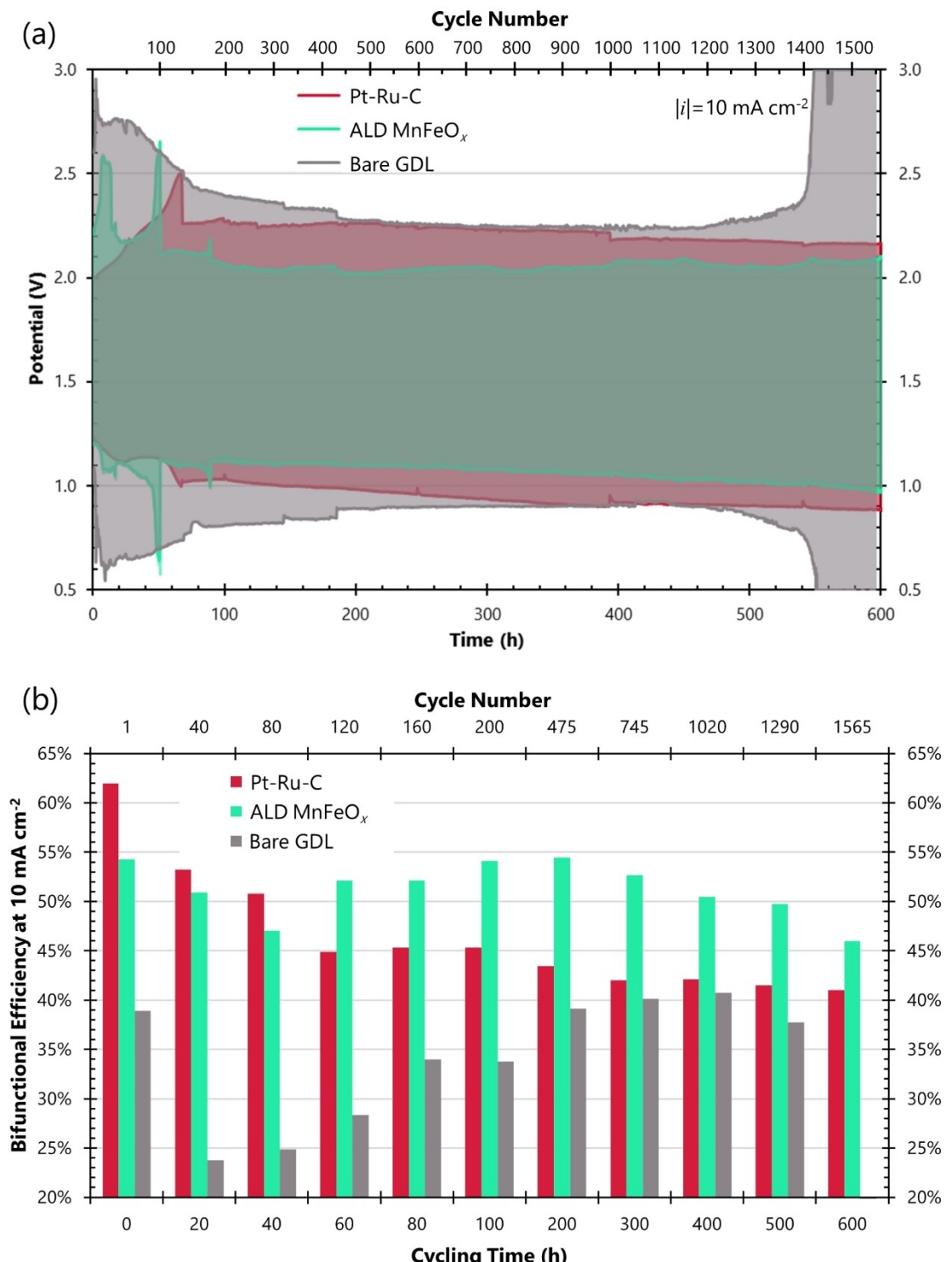


Figure 8. (a) Galvanostatic cycling of bare GDL, Pt–Ru–C, and ALD MnFeO_x. All samples are discharged and charged for 10 min at 10 mA cm⁻² for each cycle.
 (b) Bifunctional efficiency at various cycling times for bare GDL, Pt–Ru–C, and ALD MnFeO_x.

due to the dislodging of one or more bubbles within the air electrode, freeing up catalyst sites that were blocked by an oxygen bubble formed during OER.^[7]

At 54.3%, the initial bifunctional efficiency of the ALD MnFeO_x catalyst is less than that for Pt–Ru–C, but the overall degradation in bifunctional efficiency is much less for ALD

MnFeO_x. At 100 h (200 cycles) of bifunctional cycling at 10 mA cm⁻², the efficiency of ALD MnFeO_x is 54.1%, yielding an efficiency retention of 99.6%, compared with only 73.2% efficiency retention for Pt–Ru–C. Furthermore, as cycling continues for another 500 h (1290 cycles), the efficiency of ALD MnFeO_x is maintained at or above 46.0%, resulting in a final

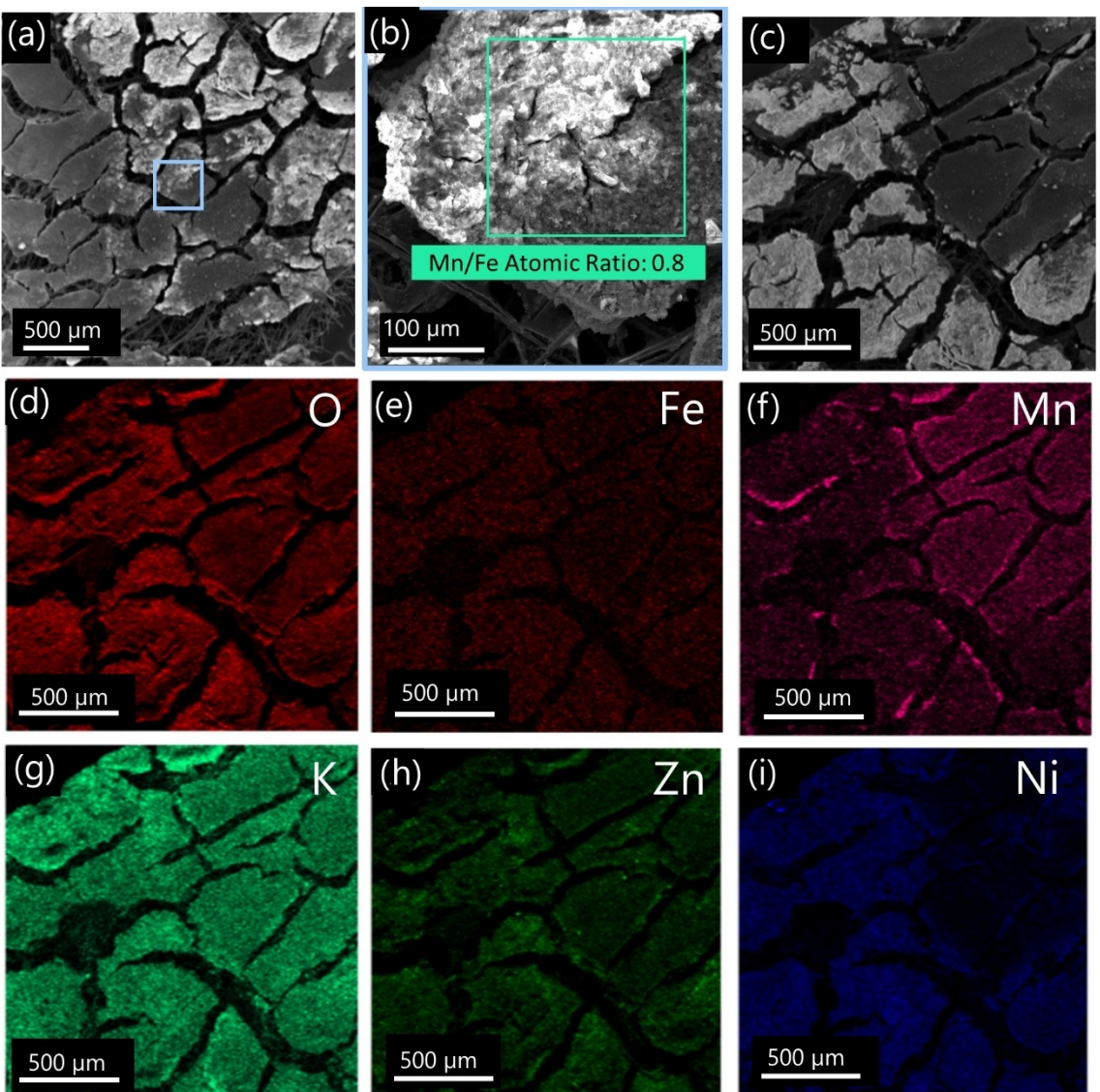


Figure 9. SEM/EDX analysis of the annealed and cycled ALD MnFeO_x coating on GDL. (a) Low-magnification secondary electron image, (b) magnified image of the indicated area in (a), with EDX of the region indicated in green providing a Mn/Fe atomic ratio of 0.8. (c) Secondary electron image taken from another region with elemental mapping of (d) O, (e) Fe, (f) Mn, (g) K, (h) Zn, and (i) Ni.

efficiency retention of 84.7% after 600 h (1565 cycles) of bifunctional cycling. Pt–Ru–C, on the other hand, has only 66.2% retention after the same period. The Pt–Ru–C catalyst, synthesized by spray-coating, suffers drastic losses in charge and discharge potential due to flooding because spray-coating only supplies the outer-most surface with catalyst material. The ALD MnFeO_x catalyst, on the other hand, displays much more stable cycling potentials because catalyst material is embedded deeper within the air electrode thickness and maintains catalytic reaction sites even after electrolyte floods into the electrode. The sharp increase in charge potential, followed by a sudden decrease in charge potential, and equivalent fluctuations in the discharge potential, for ALD MnFeO_x at around 20 h and 50 h is attributed to leaking of the ZAB cell. Once more electrolyte was added to the cell, the performance recovered. As such, the potential fluctuations do not reflect air electrode

performance but rather unresolved issues in ZAB cell design.^[51] No other accounts of cycling a ZAB using a MnFe_xO_y catalyst were found in the literature except for one report by Mathur and Halder.^[19] A ZAB prepared, via drop-casting, with their Fe-doped MnO_2 catalyst only showed 200 min of stable discharge-charge cycling, and the voltage gap at 20 mA cm^{-2} was over 3 V. Comparatively, at 20 mA cm^{-2} , the ALD MnFeO_x catalyst in this work showed only a 1.11 V voltage gap (Figure 7b). While cycling was conducted at a lower current density of 10 mA cm^{-2} , the ALD MnFeO_x ZAB in this work was able to cycle for 600 h (1565 cycles).

Also shown in Figure 8 is the cycling of bare GDL, which features an immediate loss in bifunctional efficiency within the first 20 h of cycling. However, a gradual recovery in both charge and discharge potentials is observed over the course of several hundred hours of cycling. This behaviour is attributed to proper

wetting of the air electrode by the electrolyte. Bare GDL is exceptionally hydrophobic compared with catalyst coated air electrodes and requires several cycles at high overpotential to oxidize the carbon material and improve the wettability of the electrode. This improvement in the wettability affords a larger effective surface area for the oxygen reactions and results in a lower effective current density at the electrode, improving the discharge and charge potentials. Still, the bifunctional efficiency of bare GDL is drastically inferior to any of the explored catalysts, with an initial efficiency of 38.9% and reaching only 40.7% at 400 h of cycling. At around 300 h of cycling, the charge potential of bare GDL reaches the same value as Pt–Ru–C, while the same is true for the discharge potentials at around 400 h. At this point, the Pt–Ru–C sample is no better than bare GDL and it is likely that the catalyst material has detached, oxidized, or agglomerated and is no longer effective.^[1,96,97] The ALD MnFeO_x sample, however, does not reach the same charge or discharge potential as bare GDL, demonstrating that ALD is a more robust synthesis method for long-term ZAB cycling. The bare GDL sample suddenly deteriorates and reaches the cut-off voltages of 0.5 and 3.0 V for discharge and charge, respectively, at around 550 h. The Pt–Ru–C sample, on the other hand, continues at the same potentials until 600 h.

Bifunctional cycling of the ALD FeO_x air electrode (Figure S12d) does not produce stable charge or discharge potentials and the discharge potential reaches the cut-off voltage of 0.5 V after only 135 h (300 cycles). Such poor cycling performance is due to the excessive amount of O-plasma required to grow 10 nm of FeO_x. The GDL substrate for the FeO_x sample has little to no PTFE treatment remaining and a significant amount of carbon oxidation occurs. As a result, severe flooding of the air electrode takes place and eventual electrolyte loss through the air electrode occurs. As the electrolyte level reduces in the cell, a smaller area of the electrode is exposed to the electrolyte and the current density on the electrode increases, accelerating degradation of the electrode. With the ALD MnO_x sample (Figure S12e), relatively stable cycling performance is observed up to 630 h (1645 cycles). In this case, no O-plasma reactant is required during deposition and the carbon substrate and PTFE treatment are preserved. Likewise, the ALD MnFeO_x electrode is much more stable than the ALD FeO_x sample because the MnO_x layers within the mixed deposit act as a protective layer against the aggressive ALD FeO_x steps.^[45] The occasional spike in charge or discharge potential for the ALD MnO_x sample is attributed to cell design flaws and electrolyte leaking similar to that experienced by the ALD MnFeO_x sample, where replenishing the electrolyte level recovers the potentials values completely. The bifunctional efficiency of the ALD MnO_x electrode throughout cycling (Table S6) is, in most cases, lower than that for the ALD MnFeO_x electrode, demonstrating the benefit of the mixed oxide process.

SEM of Catalyst Penetration into GDL

As a means to somewhat quantify the amount of catalyst material that penetrates into the depth of the GDL substrate during deposition, SEM and EDX analysis for the MnFeO_x and Pt–Ru–C samples was done at three locations within the GDL structure: at the surface microporous layer and at the microporous-backing layer boundary, from both the microporous side and the backing layer side. These three regions are schematically shown at the top of Figure S13. The entire GDL structure is 315 µm thick,^[21] with a microporous layer thickness of ~50 µm.^[45] The largest component of the EDX signal for all spectra in Figure S13 is C, arising from the graphite-based GDL substrate used as the air electrode. Also contained within this GDL material is PTFE, which produces a large F signal for the surface microporous layer spectra (Figures S13a and S13d). The F signal is less intense for the remaining spectra as these spectra are taken at the microporous-backing layer interface, where the backing layer has a lower PTFE loading.^[21]

Figures S13a–c show the EDX spectra for ALD MnFeO_x. The surface microporous layer (Figure S13a) has an approximately 3:1 weight ratio for Mn and Fe, and, since Mn and Fe have similar atomic masses, this value aligns with the 30:10 supercycle ratio employed during ALD. At the microporous-backing layer interface (Figures S13b and S13c), the intensity of the Mn K α peak at 5.9 keV is reduced and the Fe K α peak at 6.4 keV is eliminated entirely. The semi-quantitative analysis displays only 0.5 and 0.3 wt% of Mn for Figures S13b and S13c, respectively, down from 6.1 wt% in Figure S13a. While this may indicate an inability of the current ALD technique to deposit material within the air electrode structure, it should be emphasized that the low mass loading of ALD makes Mn and Fe detection difficult with EDX spectroscopy. Since the Mn K α peak is still visible in the spectra, it can be concluded that at least some of the precursor vapours can penetrate through the entire microporous layer of the GDL structure during ALD.

Figures S13d–f show the EDX spectra for the spray-coated Pt–Ru–C sample. Semi-quantitative analysis at the surface microporous layer (Figure S13d) shows an almost 2:1 ratio for Pt and Ru, as anticipated by the stoichiometry of the commercial powder (40 wt% Pt and 20 wt% Ru). Very weak Zn and S signals are suspected to be due to contamination of the sample but do not impact the analysis in any meaningful way. At the microporous and backing layer interface (Figures S13e and S13f), there is no detectable Pt or Ru signal, indicating that the spray-coating technique is unable to penetrate catalyst material into the depth of the GDL, accounting for the poor cycling stability of Pt–Ru–C in Figure 8. As the air electrode is flooded during prolonged cycling, the electroactive area for the oxygen reactions is shifted deeper into the GDL and towards the backing layer. Without any catalyst material present at this interface, the electrochemical activity of the spray-coated Pt–Ru–C sample becomes essentially bare GDL, as seen in Figure 8 for cycling times above 400 h.

Post-Cycling Characterization of MnFeO_x

SEM

SEM imaging of the annealed MnFeO_x sample after cycling for 600 h (1565 cycles) (Figure 9) reveals that damage occurs to the ALD coated GDL. More cracks are featured on the GDL surface, with portions of the microporous layer absent (Figures 9a–c). EDX analysis indicates a loss in Mn species, with the Mn/Fe atomic ratio reduced to ~0.8 (Figure 9b). In previous work with MnO_x ALD, the addition of an O-plasma to the deposition process resulted in an unstable MnO_x coating that dissolved during cycling.^[9] A similar phenomenon likely occurs for the ALD MnFeO_x coating in this work based on Figure 9b. Additional elements are found in the cycled sample that were not present in the uncycled annealed sample. K and Zn are most notable (Figures 9g and 9 h) and can be traced back to the ZAB electrolyte. K₂CO₃ forms when the KOH electrolyte reacts with atmospheric CO₂ or during carbon corrosion of GDL,^[5] while ZnO can precipitate from Zn containing electrolyte.^[8] A Ni current collector featured in the cell design may account for the Ni species (Figure 9i), which, like Zn, can precipitate as an oxide on the surface.

STEM

STEM analysis of the annealed ALD MnFeO_x sample after cycling for 600 h (1565 cycles) is displayed in Figure S14. As with the SEM analysis, Zn and Ni species appear in the EDX maps (Figures S14f and S14g). It is difficult to determine if the Zn and Ni are incorporated into the catalyst material, as opposed to simply surface films, since electron diffraction from post-cycling material is inconclusive and features a variety of spots/rings that correspond to both the uncycled material and a possible Zn-incorporated phase.^[9]

Conclusions

An atomic layer deposition (ALD) supercycle process for MnFe_xO_y was developed from previously established binary ALD processes for MnO_x and FeO_x. Optimization of the cycle ratio and bilayer thickness for the supercycle determined that a 30:10 mix of MnO_x and FeO_x ALD cycles provides the most catalytically active film for oxygen reduction and evolution in a Zn-air battery (ZAB). Electron microscopy analysis revealed that a homogeneously mixed ALD film uniformly encased the carbon particles of the air electrode. Electron diffraction and X-ray photoelectron spectroscopy (XPS) identified the coating as a (Mn,Fe)₃O₄ cubic spinel. The electrocatalytic activity of the bimetallic oxide ALD film in a ZAB exceeded the activity of either monometallic oxide ALD film. Long-term ZAB cycling of the ALD MnFe_xO_y catalyst yielded an efficiency retention of over 84% after 600 h (1565 cycles) at 10 mA cm⁻². A precious metal Pt–Ru–C catalyst, under the same conditions, only provided 66% efficiency retention. Energy dispersive X-ray (EDX) micro-

analysis of the bilayer air electrode structure revealed that ALD of MnFe_xO_y delivered catalyst material to regions deep within the air electrode structure. The spray-coated precious metal catalyst, however, did not penetrate into the air electrode and thus did not cycle well.

Supporting Information

Additional references have been cited within the Supporting Information.^[98–106]

Acknowledgements

M. L. would like to thank Triratna Muneshwar and Elham Rafie Borujeny (University of Alberta) for help with atomic layer deposition. D. G. I. would like to thank CanmetMATERIALS for providing access to TEM/STEM facilities. The University of Alberta NanoFAB is acknowledged for conducting XPS. Funding support was provided by the Natural Sciences and Engineering Research Council of Canada (NSERC RGPIN-2018-04488) and the University of Alberta Future Energy Systems (FES T06-P03).

Conflict of Interests

The authors declare no conflict of interest.

Data Availability Statement

The data that support the findings of this study are available in the supplementary material of this article.

Keywords: Atomic layer deposition • Catalyst • Iron • Manganese • Zn-air battery

- [1] J. Fu, Z. P. Cano, M. G. Park, A. Yu, M. Fowler, Z. Chen, *Adv. Mater.* **2017**, *29*, 1604685.
- [2] A. Dobley, T. B. Atwater, J. Passaniti, D. Carpenter, R. McKenzie, in *Linden's Handb. Batter.* (Eds.: K. W. Beard, T. B. Reddy), McGraw-Hill Education, New York, 2019.
- [3] J.-S. Lee, S. T. Kim, R. Cao, N. S. Choi, M. Liu, K. T. Lee, J. Cho, *Adv. Energy Mater.* **2011**, *1*, 34–50.
- [4] X. Chen, Z. Zhou, H. E. Karahan, Q. Shao, L. Wei, Y. Chen, *Small* **2018**, *14*, 1–29.
- [5] E. Davari, D. G. Ivey, *Sustain. Energy Fuels* **2018**, *2*, 39–67.
- [6] H. Wang, Y. Pei, K. Wang, Y. Zuo, M. Wei, J. Xiong, P. Zhang, Z. Chen, N. Shang, D. Zhong, P. Pei, *Small* **2023**, *19*, 2304863.
- [7] D. Aasen, M. P. Clark, D. G. Ivey, *Batteries & Supercaps* **2020**, *3*, 174–184.
- [8] D. Aasen, M. P. Clark, D. G. Ivey, *J. Electrochem. Soc.* **2020**, *167*, 040503.
- [9] M. P. Clark, M. Xiong, K. Cadine, D. G. Ivey, *ACS Appl. Energ. Mater.* **2020**, *3*, 603–613.
- [10] L. Han, S. Dong, E. Wang, *Adv. Mater.* **2016**, *28*, 9266–9291.
- [11] Y. Li, H. Dai, *Chem. Soc. Rev.* **2014**, *43*, 5257–5275.
- [12] J. R. Rumble, Ed., in *CRC Handb. Chem. Phys.*, CRC Press/Taylor & Francis, Boca Raton, FL, 2023.
- [13] S. Ahmed, P. A. Nelson, K. G. Gallagher, N. Susarla, D. W. Dees, *J. Power Sources* **2017**, *342*, 733–740.

- [14] C. Broicher, F. Zeng, N. Pfänder, M. Frisch, T. Bisswanger, J. Radnik, J. M. Stockmann, S. Palkovits, A. K. Beine, R. Palkovits, *ChemCatChem* **2020**, 12, 5378–5384.
- [15] J. Luo, W. H. Guo, Q. Zhang, X. H. Wang, L. Shen, H. C. Fu, L. L. Wu, X. H. Chen, H. Q. Luo, N. B. Li, *Nanoscale* **2020**, 12, 19992–20001.
- [16] Q. Zhou, Z. Su, Y. Tang, L. Ai, G. Fu, Z. Wu, D. Sun, Y. Tang, *Chem. Eur. J.* **2019**, 25, 6226–6232.
- [17] N. I. Villanueva-Martínez, C. Alegre, I. Martínez-Visús, M. J. Lázaro, *Catal. Today* **2023**, 420, 114083.
- [18] N. Bhandary, P. P. Ingole, S. Basu, *Int. J. Hydrogen Energy* **2018**, 43, 3165–3171.
- [19] A. Mathur, A. Halder, *Catal. Sci. Technol.* **2019**, 9, 1245–1254.
- [20] X. Wu, Y. Niu, B. Feng, Y. Yu, X. Huang, C. Zhong, W. Hu, C. M. Li, *ACS Appl. Mater. Interfaces* **2018**, 10, 20440–20447.
- [21] R. Schweiss, S. Hofmeister, C. Meiser, D. Dan, A. Baumann, T. Kuster, N. Haak, S. Bacher, *SGL Carbon* **2021**, 1–8, <https://www.sglcarbon.com/data/pdf/SIGRACET-Whitepaper.pdf>.
- [22] H. C. M. M. Knoops, S. E. Potts, A. A. Bol, W. M. M. Kessels, in *Handb. Cryst. Growth Thin Film. Ep.* (Ed.: T. F. Kuech), Elsevier B. V., **2015**, pp. 1101–1134.
- [23] T. Muneshwar, M. Miao, E. R. Borujeny, K. Cadien, in *Handb. Thin Film Depos.* (Eds.: K. Seshan, D. Schepis), Elsevier Inc., Cambridge, MA, **2018**, pp. 359–377.
- [24] C. D. Pham, J. P. J. Chang, M. A. Zurbuchen, J. P. J. Chang, *ACS Appl. Mater. Interfaces* **2017**, 9, 36980–36988.
- [25] A. J. M. Mackus, J. R. Schneider, C. MacIsaac, J. G. Baker, S. F. Bent, *Chem. Mater.* **2019**, 31, 1142–1183.
- [26] R. L. Puurunen, *J. Appl. Phys.* **2005**, 97, 121301.
- [27] K. Uusi-Esko, E. L. Rautama, M. Laitinen, T. Sajavaara, M. Karppinen, *Chem. Mater.* **2010**, 22, 6297–6300.
- [28] C. D. Pham, J. Chang, M. A. Zurbuchen, J. P. Chang, *Chem. Mater.* **2015**, 27, 7282–7288.
- [29] X. Li, N. C. Fan, H. J. Fan, *Chem. Vap. Depos.* **2013**, 19, 104–110.
- [30] V. Miikkulainen, A. Ruud, E. Østreng, O. Nilsen, M. Laitinen, T. Sajavaara, H. Fjellvåg, *J. Phys. Chem. C* **2014**, 118, 1258–1268.
- [31] Y. T. Chong, E. M. Y. Yau, K. Nielsch, J. Bachmann, *Chem. Mater.* **2010**, 22, 6506–6508.
- [32] A. G. Hufnagel, K. Peters, A. Müller, C. Scheu, D. Fattakhova-Rohlfing, T. Bein, *Adv. Funct. Mater.* **2016**, 26, 4435–4443.
- [33] K. Kopalko, A. Wójcik, M. Godlewski, E. Łusakowska, W. Paszkowicz, J. Z. Domagała, M. M. Godlewski, A. Szezerbakow, K. Świe,tek, K. Dybko, *Phys. Status Solidi C Conf.* **2005**, 2, 1125–1130.
- [34] X. Meng, X. Wang, D. Geng, C. Ozgit-Akgun, N. Schneider, J. W. Elam, *Mater. Horiz.* **2017**, 4, 133–154.
- [35] C. Marichy, M. Bechelany, N. Pinna, *Adv. Mater.* **2012**, 24, 1017–1032.
- [36] T. M. Onn, R. Küngas, P. Fornasiero, K. Huang, R. J. Gorte, *Inorganics* **2018**, 6, 34.
- [37] B. J. Oneill, D. H. K. Jackson, J. Lee, C. Canlas, P. C. Stair, C. L. Marshall, J. W. Elam, T. F. Kuech, J. A. Dumesic, G. W. Huber, *ACS Catal.* **2015**, 5, 1804–1825.
- [38] Q. Wang, H. Liang, J. Zhou, J. Wang, Z. Ye, M. Zhao, H. Yang, Y. Song, J. Guo, *Chem. Eng. J.* **2023**, 467, 143482.
- [39] X. Shi, B. He, L. Zhao, Y. Gong, R. Wang, H. Wang, *J. Power Sources* **2021**, 482, 228955.
- [40] P. Chu, Y. Zhang, J. He, J. Chen, J. Zhuang, Y. Li, X. Ren, P. Zhang, L. Sun, B. Yu, S. Chen, *Small Methods* **2022**, 6, 4–11.
- [41] A. Seong, J. Kim, O. Kwon, H. Y. Jeong, R. J. Gorte, J. M. Vohs, G. Kim, *Nano Energy* **2020**, 71, 104564.
- [42] H. Li, Z. Guo, X. Wang, *J. Mater. Chem. A* **2017**, 5, 21353–21361.
- [43] S. Yan, H. Li, J. Zhu, W. Xiong, R. Lei, X. Wang, *Nanotechnology* **2021**, 32, 275402.
- [44] M. P. Clark, T. Muneshwar, M. Xiong, K. Cadien, D. G. Ivey, *ACS Appl. Nano Mater.* **2019**, 2, 267–277.
- [45] M. Labbe, M. P. Clark, Z. Abedi, A. He, K. Cadien, D. G. Ivey, *Surf. Coat. Technol.* **2021**, 421, 127390.
- [46] T. Muneshwar, K. Cadien, *J. Vac. Sci. Technol. A Vacuum, Surfaces, Film.* **2015**, 33, 031502.
- [47] M. Ritala, J. Niinistö, in *Chem. Vap. Depos.* (Eds.: A. C. Jones, M. L. Hitchman), Royal Society Of Chemistry, Cambridge, UK, **2009**, pp. 158–206.
- [48] T. Muneshwar, K. Cadien, *Appl. Surf. Sci.* **2015**, 328, 344–348.
- [49] M. Labbe, K. Cadien, D. G. Ivey, *J. Phys. Chem. C* **2022**, 126, 19883–19894.
- [50] D. Aasen, M. Clark, D. G. Ivey, *Batteries & Supercaps* **2019**, 2, 882–893.
- [51] M. Labbe, D. G. Ivey, *J. Electrochem. Soc.* **2023**, 170, 090515.
- [52] D. A. Shirley, *Phys. Rev. B* **1972**, 5, 4709–4714.
- [53] M. C. Biesinger, B. P. Payne, A. P. Grosvenor, L. W. M. Lau, A. R. Gerson, R. S. C. Smart, *Appl. Surf. Sci.* **2011**, 257, 2717–2730.
- [54] M. Chigane, M. Ishikawa, *J. Electrochem. Soc.* **2000**, 147, 2246.
- [55] Y. Gorlin, B. Lassalle-Kaiser, J. D. Benck, S. Gul, S. M. Webb, V. K. Yachandra, J. Yano, T. F. Jaramillo, *J. Am. Chem. Soc.* **2013**, 135, 8525–8534.
- [56] F. Visentin, R. Gerbasi, G. Rossetto, C. De Zorzi, N. El Habra, D. Barreca, A. Gasparotto, *Surf. Sci. Spectra* **2011**, 18, 29–35.
- [57] Y. Meng, W. Song, H. Huang, Z. Ren, S. Y. Chen, S. L. Suib, *J. Am. Chem. Soc.* **2014**, 136, 11452–11464.
- [58] A. McDougall, Z. Abedi, D. G. Ivey, *J. Appl. Electrochem.* **2022**, 52, 437–459.
- [59] M. Xiong, M. P. Clark, M. Labbe, D. G. Ivey, *J. Power Sources* **2018**, 393, 108–118.
- [60] Y. Leng, *Mater. Charact.* Wiley-VCH, Weinheim, Germany, **2013**.
- [61] C. Detavernier, J. Dendooven, S. Pulinthanthu Sree, K. F. Ludwig, J. A. Martens, *Chem. Soc. Rev.* **2011**, 40, 5242–5253.
- [62] Z. Guo, L. Tan, *Fundamentals and Applications of Nanomaterials*, Artech House, Norwood, MA, **2009**.
- [63] B. P. Payne, M. C. Biesinger, N. S. McIntyre, *J. Electron Spectrosc. Relat. Phenom.* **2012**, 185, 159–166.
- [64] M. Chigane, M. Ishikawa, M. Izaki, *J. Electrochem. Soc.* **2001**, 148, D96.
- [65] B. P. Payne, M. C. Biesinger, N. S. McIntyre, *J. Electron Spectrosc. Relat. Phenom.* **2009**, 175, 55–65.
- [66] J. Jia, P. Zhang, L. Chen, *Appl. Catal. B* **2016**, 189, 210–218.
- [67] T. Zhang, Z. Li, L. Wang, Z. Zhang, S. Wang, *Int. J. Hydrogen Energy* **2019**, 44, 1610–1619.
- [68] J. L. Hueso, J. P. Espinós, A. Caballero, J. Cotrino, A. R. González-Elipe, *Carbon* **2007**, 45, 89–96.
- [69] F. A. Stevie, C. L. Donley, *J. Vac. Sci. Technol. A* **2020**, 38, 063204.
- [70] A. P. Grosvenor, B. A. Kobe, M. C. Biesinger, N. S. McIntyre, *Surf. Interface Anal.* **2004**, 36, 1564–1574.
- [71] D. A. Aasen, Y. Shen, D. G. Ivey, *ChemElectroChem* **2020**, 7, 2283–2296.
- [72] T. Yamashita, P. Hayes, *Appl. Surf. Sci.* **2008**, 254, 2441–2449.
- [73] D. D. Hawn, B. M. DeKoven, *Surf. Interface Anal.* **1987**, 10, 63–74.
- [74] E. S. Ilton, J. F. Post, P. J. Heaney, F. T. Ling, S. N. Kerisit, *Appl. Surf. Sci.* **2016**, 366, 475–485.
- [75] S. Ardizzone, C. L. Bianchi, D. Tirelli, *Colloids Surf. A* **1998**, 134, 305–312.
- [76] M. Oku, K. Hirokawa, S. Ikeda, *J. Electron Spectrosc. Relat. Phenom.* **1975**, 7, 465–473.
- [77] J. F. Moulder, W. F. Stickle, P. E. Sobol, K. D. Bomben, *Handbook of X-Ray Photoelectron Spectroscopy*, Perkin-Elmer Corporation, Eden Prairie, MN, **1992**.
- [78] M. Oku, K. Wagatsuma, T. Konishi, *J. Electron Spectrosc. Relat. Phenom.* **1999**, 98–99, 277–285.
- [79] J. Gao, C. Jia, L. Zhang, H. Wang, Y. Yang, S. F. Hung, Y. Y. Hsu, B. Liu, *J. Catal.* **2016**, 341, 82–90.
- [80] V. R. Galakhov, M. Demeter, S. Bartkowski, M. Neumann, N. A. Ovechkina, E. Z. Kurmaev, N. I. Lobachevskaya, Y. M. Mukovskii, J. Mitchell, D. L. Ederer, *Phys. Rev. B: Condens. Matter Mater. Phys.* **2002**, 65, 1–4.
- [81] V. Di Castro, G. Polzonetti, *J. Electron Spectrosc. Relat. Phenom.* **1989**, 48, 117–123.
- [82] J. S. Foord, R. B. Jackman, G. C. Allen, *Philos. Mag. A Phys. Condens. Matter, Struct. Defects Mech. Prop.* **1984**, 49, 657–663.
- [83] H. J. T. Ellingham, *J. Soc. Chem. Ind.* **1944**, 63, 125–144.
- [84] S. Pétigny, H. Mostéfa-Sba, B. Domenichini, E. Lesniewska, A. Steinbrunn, S. Bourgeois, *Surf. Sci.* **1998**, 410, 250–257.
- [85] S. Hashimoto, K. Hirokawa, Y. Fukuda, K. Suzuki, T. Suzuki, N. Usuki, N. Gennai, S. Yoshida, M. Koda, H. Sezaki, H. Horie, A. Tanaka, T. Ohtsubo, *Surf. Interface Anal.* **1992**, 18, 799–806.
- [86] T. Battault, R. Legros, A. Rousset, *J. Eur. Ceram. Soc.* **1995**, 15, 1141–1147.
- [87] Y. Zhan, C. Xu, M. Lu, Z. Liu, J. Y. Lee, *J. Mater. Chem. A* **2014**, 2, 16217–16223.
- [88] V. Baron, J. Gutzmer, H. Rundlöf, R. Tellgren, *Am. Mineral.* **1998**, 83, 786–793.
- [89] Q. Zhao, Z. Yan, C. Chen, J. Chen, *Chem. Rev.* **2017**, 117, 10121–10211.
- [90] C. Li, X. Han, F. Cheng, Y. Hu, C. Chen, J. Chen, *Nat. Commun.* **2015**, 6, 4–11.
- [91] S. Hirai, S. Yagi, A. Seno, M. Fujioka, T. Ohno, T. Matsuda, *RSC Adv.* **2016**, 6, 2019–2023.
- [92] I. Roche, E. Chaînet, M. Chatenet, J. Vondrák, *J. Appl. Electrochem.* **2008**, 38, 1195–1201.

- [93] I. Roche, E. Chaînet, M. Chatenet, J. Vondrák, *J. Phys. Chem. C* **2007**, *111*, 1434–1443.
- [94] J. Vondrák, B. Klápník, J. Velická, M. Sedláříková, J. Reiter, I. Roche, E. Chaînet, J. F. Fauvarque, M. Chatenet, *J. New Mater. Electrochem. Syst.* **2005**, *8*, 209–212.
- [95] R. D. L. Smith, M. S. Prévot, R. D. Fagan, S. Trudel, C. P. Berlinguette, M. S. Pre, R. D. Fagan, S. Trudel, *J. Am. Chem. Soc.* **2013**, *135*, 11580–11586.
- [96] S. Guo, S. Zhang, S. Sun, *Angew. Chem. Int. Ed.* **2013**, *52*, 8526–8544.
- [97] N. Zamel, *J. Power Sources* **2016**, *309*, 141–159.
- [98] S. M. George, *Chem. Rev.* **2010**, *110*, 111–131.
- [99] J. W. Elam, D. Routkevitch, P. P. Mardilovich, S. M. George, *Chem. Mater.* **2003**, *15*, 3507–3517.
- [100] M. Ritala, M. Leskela, in *Handb. Thin Film Mater.* (Ed.: H. S. Nalwa), Academic Press, San Diego, CA, **2002**, pp. 103–159.
- [101] M. Xiong, D. G. Ivey, *Batteries & Supercaps* **2019**, *2*, 326–335.
- [102] J. A. Conesa, R. Font, *Polym. Eng. Sci.* **2001**, *41*, 2137–2147.
- [103] J. T. Titantah, D. Lamoen, *Diamond Relat. Mater.* **2007**, *16*, 581–588.
- [104] A. P. Dementjev, A. De Graaf, M. C. M. Van de Sanden, K. I. Maslakov, A. V. Naumkin, A. A. Serov, *Diamond Relat. Mater.* **2000**, *9*, 1904–1907.
- [105] C. Chen, Y. Li, D. Cheng, H. He, K. Zhou, *ACS Appl. Mater. Interfaces* **2020**, *12*, 40415–40425.
- [106] Y. Zhong, J. Dai, X. Xu, C. Su, Z. Shao, *ChemElectroChem* **2020**, *7*, 4949–4955.

Manuscript received: February 29, 2024

Revised manuscript received: May 22, 2024

Accepted manuscript online: May 31, 2024

Version of record online: July 5, 2024